P-ISSN 0126-3188
E-ISSN 2443-3926

BRIN
BADAN RISET
DAN INOVASI NASIONAL

METALURGI

VOLUME 39 No 2 2024

SCIENTIFIC JOURNAL ACCREDITATION NO.3/E/KPT/2019

National Research and Innovation Agency

Publisher :
National Research and Innovation Agency (BRIN)
KST B.J Habibie Serpong, Tangerang Selatan, Banten, Indonesia, 15314

E-mail: metalurgi@brin.go.id

Science and technology magazine, regularly published every year; one volume consists of 3 editions

METALURGI

VOLUME 39 NUMBER 2 2024

P-ISSN 0126-3188
E-ISSN 2443-3926

ACCREDITATION: SK No. 72/E/KPT/2024

PREFACE

The author gives thanks to Allah for bestowing His blessing and direction, allowing the **Metalurgi Journal Volume 39, Edition 2**, **2024** to be successfully published.

The first article results from Sri Mulyati Latifa and colleagues' research activities on the *Synthesis of Mesoporous Nickel using Electrodeposition Method*. Agsel Fauzia Hakim and colleagues presented the second article, *Study of Iron and Calcium Removal on Manganese Sulfate Precursors for Battery Cathode Raw Material Applications*. Fionna Angellinnov and colleagues investigated the *Optimization of NMC811 Synthesis via Oxalate Coprecipitation Method for Lithium-ion Battery Cathodein* the following article. For the fourth article, Fakhrudin Yudomustafa and colleagues studied *Study on Leaching Lanthanum from Ferronickel Slag with Pretreatment Alkaline Fusion*. The fifth article by Kurotun Aini and her colleagues discussed a *The Effect of Single and Double-Doped Addition on 8YSZ Coating Layers Deposited on Inconel 625 by Electrophoretic Deposition*.

The publication of this volume in the Metalurgi Journal will benefit the advancement of research in Indonesia.

EDITORIAL

METALURGI

ISSN 0126 – 3188 Vol. 39 No. 2, 2024

Keywords sourced from articles. This abstract is reproduced without permission or fee.

Sri Mulyati Latifah[a], Mochamad Ghais Vito[a], Djoko Hadi Prajitno[b] ([a]Metallurgical Engineering, General Achmad Yani University, [b]Research Center for Radiation Process of Technology, National Research and Innovation Agency (BRIN))

Metalurgi, Vol. 39 No. 2, 2024

Synthesis of Mesoporous Nickel using Electrodeposition Method

Mesoporous material technology has recently become increasingly popular among scientists and industry professionals. Electrodeposition is a metal deposition process that employs an electric current. The most typical applications of electrodeposition are metal coating (electroplating) and the creation of porous materials. This study aimed to analyze the effects of current and nickel synthesis time on the formation of mesoporous nickel morphology using corn starch. The method for producing mesoporous nickel deposits uses an electrodeposition process using corn starch additives. The process of making mesoporous nickel varies at currents of 4, 5, and 6 A, holding times of 3, 4, and 5 hours, and additional weights of corn starch of 1, 2, and 3 g, with the weight of nickel deposits produced being 1.19, 1.3, and 1.9 g, with an increase in nickel deposits from currents of 4 to 6 A (holding time of 3 to 5 hours) of 0.71 g (59.66%). The smallest pore diameter of 112 nm was obtained using a current of 6 A, a holding time of 5 hours, with 3 g of corn starch. Characterization was carried out on the electrodeposition layer using XRD (x-ray diffraction) and SEM-EDS (scanning electron microscope-energy dispersive spectroscopy), where the results of the XRD analysis showed the presence of α-Ni, Y-Fe, and Fe_1Ni_3 *compounds, and the results of SEM-EDS showed porous Ni deposits with the highest Ni concentration above 80%. The bigger the current employed and the holding period in the electrodeposition process, the heavier the Ni deposit formed*

Keywords: Mesoporous, electrodeposition, nickel, α*-Ni,* Fe_1Ni_3 *compounds*

METALURGI

ISSN 0126 – 3188 Vol. 39 No. 2, 2024

Keywords sourced from articles. This abstract is reproduced without permission or fee.

Agsel Fauzia Hakim[a], Lia Andriyah[b], Soesaptri Oediyani[a], Latifa Hanum Lalasari[b], Eko Sulistiyono[b], Januar Irawan[b], Tri Arini[b], Fariza Eka Yunita[b], Ariyo Suharyanto[b], Iwan Setiawan[b], Florentinus Firdiyono[b], Akhmad Herman Yuwono[c,d] ([a]Department of Metallurgy, Sultan Ageng Tirtayasa University; [b]Research Center for Metallurgy, National Research and Innovation Agency (BRIN) ; [c]Department of Metallurgical and Materials Engineering, University of Indonesia; [d]Advanced Materials Research Center, University of Indonesia)

Metalurgi, Vol. 39 No. 2, 2024

Study of Iron and Calcium Removal on Manganese Sulfate Precursors for Battery Cathode Raw Material Applications

Global battery sales are expected to reach $310.8 billion in 2027, up 14.1% from 2020. 95% of the world's batteries are lead-acid, lithium-ion, or nickel-based. One of the most popular batteries on the global market is lithium-ion, which uses MnSO4 powder as its cathode raw material. Manganese sulfate-based lithium-ion batteries can be made using Indonesian resources, specifically manganese ore from Trenggalek. Trenggalek manganese ore is of poor quality and contains impurities, primarily Fe and Ca. To produce 98% powder manganese sulfate, the solution is prepared, reduced with briquette charcoal, leached, precipitated, carbonated, and crystallised. NH_4OH *reagent is used to remove Fe through precipitation, and the carbonatation process is employed to eliminate Ca, resulting in 97.237% purity of manganese sulfate powder product. This outcome is achieved under precipitation process conditions of* $[NH_4OH\ 2M]$, $T = 80\ °C$, $pH = 4$, $t = 180$ *minutes, while carbonatation process conditions are* $T=50\ °C$, $t = 120$ *minutes.*

Keywords: Lithium-ion batteries, iron recipitation, carbonatation, manganese sulphate

METALURGI

ISSN 0126 – 3188 Vol. 39 No. 2, 2024

Keywords sourced from articles. This abstract is reproduced without permission or fee.

Fiona Angellinnov[a], Achmad Subhan[b], Bambang Priyono[a,c], and Anne Zulfia Syahrial[a,c] **(**[a]Department of Metallurgical and Materials Engineering, University of Indonesia; [b]Research Center for Advanced Materials, National Research and Innovation Agency (BRIN); [c]Tropical Renewable Energy Centre, University of Indonesia)

Metalurgi, Vol. 39 No. 2, 2024

Optimization of NMC811 Synthesis via Oxalate Coprecipitation Method for Lithium-Ion Battery Cathode

NMC811 was synthesized through the oxalate coprecipitation method, followed by the solid-state method of lithiation. ***.*** *Stirring speed (500, 750, 1000 rpm), aging time (0, 3, 5 h), sintering atmosphere (with and without oxygen flow), sintering temperature (700, 750, 800 °C), and lithium concentration (0, 2, 5% excess) effect on the NMC811 were examined. Characterization results showed that the optimum stirring speed and aging time are 750 rpm and 3 hours. Based on structural analysis, the best condition for sintering is in oxygen atmospheres at 800 °C with a lithium concentration of 2% excess. NMC811, synthesized with these optimum parameters, provided a 212.93 mAh/g capacity. These findings deliver insight into NMC811 synthesis optimization.*

Keywords: Cathode material, oxalate coprecipitation, NMC811, synthesis method

METALURGI

ISSN 0126 – 3188 Vol. 39 No. 2, 2024

Keywords sourced from articles. This abstract is reproduced without permission or fee.

Fakhruddin Yudomustafa[1], Eni Febriana[2], Wahyu Mayangsari[2], Nurhayati Indah Ciptasari[2], Ari Yustisia Akbar[2], Hendrik[2], Soesaptri Oediyani[1] and Agus Budi Prasetyo[2] ([1]Department of Metallurgy, Sultan Ageng Tirtayasa University; [2]Research Center for Metallurgy, National Research and Innovation Agency (BRIN))

Metalurgi, Vol. 39 No. 2, 2024

Study on Leaching Lanthanum from Ferronickel Slag with Pretreatment Alkali Fusion

Ferronickel slag is a byproduct of nickel ore smelting. Several efforts have been made to find alternative applications for ferronickel slag, such as the production of construction materials, cement, or geopolymers. It is reported that 38% is used for road construction, 48% is used for industrial cement mixtures, and the rest is used for fertilizers, geopolymers, and hydraulic techniques. Ferronickel slag still contains some valuable minerals such as silica, magnesium, nickel, iron, and several REEs (rare earth elements). One of the REEs, namely lanthanum, has many applications, including Ni-MH (nickel-metal hydride) batteries, phosphors for lamps, fluid-cracking catalysts for oil refining, LaNi5 for hydrogen gas storage, metal alloys for cast iron, steel and magnesium alloys, additives for glassware (for cameras), and lanthanum hexaboride ceramic. In connection with the slag, which contains impurities in strong silica compounds, it is necessary to carry out an alkaline fusion treatment. Alkaline fusion was carried out by varying the time from 0.5 to 4 hours and the ratio of the mass of slag to NaOH: 1:0.6, 1:1, 1:1.23, 1:1.47, and 1:1.84. The biggest decrease in SiO_2 *was in the 3-hour alkaline fusion time, from 48.347% to 27.3%, and in the mass ratio at 1:1.47, from 48.347% to 21.413%. This research aims to provide added value for ferronickel slag by extracting lanthanum by acid leaching using* H_2SO_4 *reagent by varying the time (5, 10, 30, 60, and 120 minutes), temperature (30, 60, and 90 °C), and concentration (1, 2, and 3 M). The results showed that the best leaching point was at 5 minutes, 30 °C, and 1 M, yielding a lanthanum extraction percentage of 38.082%.*

Keywords: Acid leaching, added value, alkali fusion, ferronickel slag, lanthanum

METALURGI

ISSN 0126 – 3188 Vol. 39 No. 2, 2024

UDC (OXDCF)

Kurotun Aini[1,2], Fina Fitratun Amaliyah[1], Eni Sugiarti[2], Resetiana Dwi Desiati[2], Nurul Latifah[2], Safitry Ramandhany[2], Ihah Fadilah[2], and Aunillah Putri El Nasihah[2] ([1]Department of Physics, Faculty of Science and Technology, State Islamic University Sultan Maulana Hasanuddin Banten; [2]Research Center for Advanced Materials, National Research and Innovation Agency (BRIN))

Metalurgi, Vol. 39 No. 2, 2024

The Effect of Single and Double-Doped Addition on 8YSZ Coating Layers Deposited on Inconel 625 by Electrophoretic Deposition

The ceramic layers of 8 mol% yttria-stabilized zirconia (8YSZ), singly doped with Fe2O3 and doubly doped with Fe2O3 and Al2O3, have been deposited successfully on Inconel 625 substrates by the EPD (electrophoretic deposition) process. The oxide doping influenced the stability of the EPD suspension and affected the density of the resultant layer. To improve the adhesion between the layer and the substrate, a two-step sintering was performed up to 1200 ºC for a total duration of 4 hours in a horizontal vacuum furnace, with a heating rate of 2 ºC per minute in an Argon gas atmosphere. FE-SEM (field emission scanning electron microscopy) and vickers hardness tests were employed to investigate the effect of single and double doping on the morphology and hardness of the coating layers, respectively. EDS (energy dispersive spectroscopy) was employed to analyze the elemental composition of the layers, while XRD (x-ray diffractometry) was utilized to determine the crystalline phases. The results indicated that the double-doped coating sample possesses a better microstructure, and the layer with double doping exhibits a denser microstructure and reduced porosity (3.84%) in contrast to the single-doping layer (6.05%). The vickers hardness test indicates a rise in hardness from 65.3 HV with single doping to 283.78 HV with double-doping layers, due to the presence of Al2O3 as the interstitial agent, which reduces the layer's porosity and enhances adhesion between the layer and the substrate. Furthermore, the addition of Al¬2O3 as the double dopant may impede the t□ m phase transformation, leading to enhanced thermal stability in the double-doped coating sample compared to the single-doped coating sample. This study shows that double-doping techniques can improve the efficiency of ceramic coatings for high-temperature applications, such as gas turbine components, and also gives opportunities for more research in oxidation, corrosion, and erosion testing.

Keywords: Al_2O_3*, electrophoretic deposition,* Fe_2O_3*, inconel 625, yttrium-stabilized zirconia*

Metalurgi (2024) 2: 63 - 72

METALURGI
Majalah Ilmu dan Teknologi
p-ISSN 0126-3188 | e-ISSN 2443-3926
ejurnalmaterialmetalurgi.lipi.go.id

SYNTHESIS OF MESOPOROUS NICKEL USING ELECTRODEPOSITION METHOD

Sri Mulyati Latifah[a*], Mochamad Ghais Vito[a], Djoko Hadi Prajitno[b]
[a]Metallurgical Engineering, General Achmad Yani University
Jl. Ters. Jenderal Gatot Subroto PO BOX 807 Bandung, Indonesia 40285
[b]Research Center for Radiation Process of Technology, National Research and Innovation Agency (BRIN)
Jl. Tamansari No 71, Bandung, Indonesia 40317
*E-mail: sri.mulyati@lecture.unjani.acid

Received: 08-03-2024, Revised: 29-07-2024, Accepted: 14-08-2024

Abstract

Mesoporous material technology has recently become increasingly popular among scientists and industry professionals. Electrodeposition is a metal deposition process that employs an electric current. The most typical applications of electrodeposition are metal coating (electroplating) and the creation of porous materials. This study aimed to analyze the effects of current and nickel synthesis time on the formation of mesoporous nickel morphology using corn starch. The method for producing mesoporous nickel deposits uses an electrodeposition process using corn starch additives. The process of making mesoporous nickel varies at currents of 4, 5, and 6 A, holding times of 3, 4, and 5 hours, and additional weights of corn starch of 1, 2, and 3 g, with the weight of nickel deposits produced being 1.19, 1.3, and 1.9 g, with an increase in nickel deposits from currents of 4 to 6 A (holding time of 3 to 5 hours) of 0.71 g (59.66%). The smallest pore diameter of 112 nm was obtained using a current of 6 A, a holding time of 5 hours, with 3 g of corn starch. Characterization was carried out on the electrodeposition layer using XRD (x-ray diffraction) and SEM-EDS (scanning electron microscope-energy dispersive spectroscopy), where the results of the XRD analysis showed the presence of α-Ni, Ɣ-Fe, and Fe_1Ni_3 *compounds, and the results of SEM-EDS showed porous Ni deposits with the highest Ni concentration above 80%. The bigger the current employed and the holding period in the electrodeposition process, the heavier the Ni deposit formed.*

Keywords: *Mesoporous, electrodeposition, nickel, α-Ni,* Fe_1Ni_3 *compounds*

1. INTRODUCTION

The study of porous materials has attracted the curiosity of scientists and engineers alike. Compared with solid metals, porous metals have low density, large specific surface area (large specific surface area), good energy absorption, and greater specific strength and stiffness. The open-cell porous metal has good heat exchange, radiation properties**,** sound absorption, and permeation and infiltration properties [1].

Mesoporous nickel is an excellent sound-absorbing material, especially at high frequencies. Designing a sound absorption structure can increase sound absorption performance in low frequencies. Nickel foam is also one of the best electrode materials for making cadmium-nickel batteries, hydrogen-nickel batteries, and filtration materials. In addition, nickel is widely used for high-temperature materials, so it is commonly used in industrial applications.

Development of monoatomic Ni metal electrocatalysts supported by triazine-based controllable microporous carbon nanospheres (Ni SAcs/McNPs) and the catalysis was prepared using a self-assembly strategy of aqueous lotion polymerization. The catalyst can function effectively in strong alkaline electrolyte solutions [2]-[3]. Furthermore, in the latest research in the present work, ordered mesoporous silica containing Ni atoms as active sites was synthesized by a new low-temperature

DOI: 10.55981/metalurgi.2024.704

Metalurgi is Sinta 2 Journal (https://sinta.kemdikbud.go.id/journals/profile/3708) accredited by Ministry of Education, Culture, Research, and Technology, Republic Indonesia

condensation of silica precursors on a micellar template from aqueous solutions in the presence of nickel salt [4]. This method is advantageous because it avoids high temperatures or hazardous organic solvents, making it more environmentally friendly [4]. Further research on the formation of 2D mesoporous has shown additional structural functions with great potential in electrocatalysis that enhance electrocatalytic activity and stability and optimize electrocatalytic selectivity [5]. A popular new approach involves using ordered mesoporous silica as a pattern, where nickel is incorporated into the silica framework [6]. And then researchers also explored the nanocasting technique, where mesoporous nickel is made by infiltrating nickel precursors into the pattern, which are then removed, leaving a porous nickel structure. This technique allows high control over the porosity and surface area of the material [6].

Recent research explores different methods of synthesizing mesoporous nickel, such as silica templates, which allow precise control over pore size and structure. This ensures a uniform distribution of active nickel sites, improving the material's filtration and catalysis efficiency.

Porous materials can be made by mixing metal powder with a blowing agent and compacting the mixture (compaction), and one of them is EDP (electrodeposition) [6].

Electrochemical deposition, or electrodeposition, is explained for the fabrication and mass production of functional and nanostructured device materials. As basic information for understanding the concepts used to nanostructure electrodeposited materials, reviewing electrodeposition constituents, thermodynamics and kinetics of electrodeposition, electrochemical and instrumental assessment techniques, as well as other physical factors influencing electrodeposition [7]. Electrodeposition is often fabricated with wire electrolytes because the resulting pore structure is bi-continuous and has a very high surface area-to-volume ratio [8]. Electrodeposition not only uses ferrous or non-ferrous matrices, but also composites, which are renowned as an excellent approach for creating metal matrix composite layers. It contains finely scattered inert particles [9]. However, electrodeposition does not only use sulfate and chloride solutions; it also uses a thin layer of silicon (Si) to replace other Si wafer formation techniques known as silicon electrodeposition predecessors [10].

Electrodeposition (EDP) has been the main method of coating metals for various applications for nearly 100 years. Its popularity is due to its straightforward design, low cost, uniform yield, and successful application of various metals and substrates [6]. Many factors have been shown to influence the composition, texture, and chemical properties of the resulting precipitate, such as current density, nature and concentration of metal ions, solution temperature, composition, the waveform of the applied current, substrate surface, and agitation. In particular, additives play a complex role in metal deposition due to their ability to greatly alter the growth mechanism and structure of the resulting precipitate[2],[9],[11].

Meanwhile, the novelty in this study is the Ni electrodeposition process, which is given a catalyst in the form of corn starch to form Ni pores on the surface with uniform and homogeneous mesopore sizes. However, additives must be used to open the porous layer. Corn starch as an additive in the electrodeposition process is usually associated with its use as a binder or particle binder in the manufacture of electrodes or coating certain materials on the surface of the substrate. This method is generally known as porous electrodeposition or template electrodeposition. Corn starch is a mold material that will provide a porous structure to the deposited material. Therefore, this study aimed to analyze the effects of nickel synthesis current and time on the formation of mesoporous nickel morphology using corn starch additives or catalysts.

2. MATERIALS AND METHODS

The materials used for the electrodeposition process are ST 37 steel as the cathode, and 99% purity nickel plate as the anode. Electrodeposition solution materials use 32% technical HCl solution from Kimiamart products, technical NaOH crystal solids from Kimiamart products, technical H_2SO_4 solution with 94% purity from Kimiamart products, technical $NiSO_46H_2O$ powder from Bratachem products, and distilled water (*aqueous*) and the cornstarch used is a commercial product with 100% purity from the Maizenaku brand as an additive Cornstarch is primarily composed of carbohydrates, which consist of carbon, hydrogen, and oxygen. Nitrogen content in pure cornstarch is typically very low or negligible due to Carbon (C): Approximately 44-45%, Hydrogen (H): Approximately 6-7%, Nitrogen (N): Typically very low, often below 0.5% with elements are Na, K, Ca, Mg, P, S, Fe, Zn and Cu [10]. The tools used for the process of making Ni shafts in this research are an analytical balance, chemical beaker, measuring cup, measuring pipette, spatula, measuring flask, stir bar, spray bottle, dryer, and ampere meter [12].

Before the electrodeposition process, a 1 M $NiSO_4$ electrolyte solution was made, and an additive (*corn starch*) was added. A mixing process followed this until the solution was homogeneous, which was then vibrated for 30 minutes using an ultrasonic device. These additives are intended to form a medium for porous materials, and the ultrasonic process aims to prevent oligomerization (clumping) from forming.

Electrodeposition layer thickness is achieved by depositing a material (usually metal) onto an electrode using an electric current. The amount of material deposited on an electrode can be calculated using a combination of Faraday's first and second laws of electrolysis [13].

$$m = \frac{M \, x \, I \, x \, t}{n \, x \, F} \quad (1)$$

Where: m is the mass of the substance deposited (g), M is the molar mass of the substance (g/mol), I is the current in amperes (A), t is the time in seconds (s), n is the number of electrons transferred (valency), F is Faraday's constant = 96,485 C/mol [13].

The EDP (electrodeposition procedure) process was carried out following the ultrasonic process by injecting 1 M $NiSO_4$ electrolyte solution into a beaker, followed by a succession of electrolysis operations as shown in Fig. 1 [2],[9]. The EDP experiment used process parameters, namely the concentration of electrolyte solution, cathode (workpiece), anode Ni plate (pure Ni), current, and time.

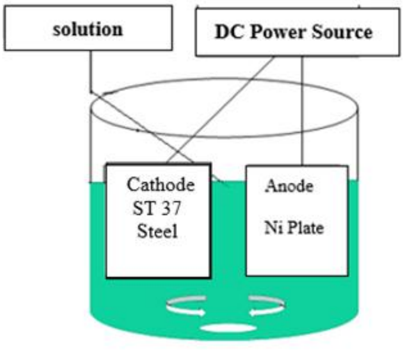

Figure 1. The series of electrodeposition processes

The EDP procedure began by applying an electric current of 4, 5, and 6 A for 3, 4, and 5 hours, respectively, and then adding 1, 2, and 3 g of additives to achieve the best porous sediment outcomes. This electrolysis procedure was carried out by providing an external current, and a direct current source connected in series with an ammeter, and the electrodeposition process took place at a temperature of 25 °C. After electrodeposition, the cathode was removed and rinsed with distilled water (aquades) and then dried in the open air using a hairdryer.

To create a porous material, the cathode was heated in a tube furnace for approximately 30 minutes at room temperature to 275 °C. This caused the nickel layer to peel off and the corn starch to evaporate.

In this study, testing and characterization of nickel mesoporous deposits from the electrodeposition process were carried out using visual inspection, XRD (x-ray diffraction), and SEM (scanning electron microscope) equipped with EDS (energy dispersive x-ray spectroscopy) characterization [8]-[10]. The visual inspection method uses sunlight and the human eye. The machine tools used for XRD characterization were SmartLab, the Rigaku Ultima IV (Cu-Source) brand, where XRD testing was carried out on mesoporous nickel, which underwent an electrodeposition process, with a current of 4A and a time of 3 hours. The SEM-EDS characterization was a Hitachi SU 3500.

3. RESULTS AND DISCUSSION

3.1 Electrodeposition Process

Figure 2 depicts the effects of the electrodeposition process on the weight of the deposit formed during EDP (electrodeposition) as time and current adjustments were applied. Figure 2 illustrates a graph of the effect of time on the weight of realistic deposits created using the electrodeposition procedure. Nickel deposits were produced using electrodeposition at holding times of 3, 4, and 5 hours and currents of 4, 5, and 6 A, respectively. The nickel deposits were 1.19, 1.3, and 1.9 g.

This research showed an increase in the weight of nickel deposits from a current of 4A to 5A (holding time 3 to 4 hours), weighing 0.11 g (9.24%). And the increase in nickel deposits also occurred from a current of 4A to 6 A (with a standing time of 3 to 5 hours) with a weight of 0.71 g (59.66%), for an additional current of 5 to 6 A with a holding time of 4 to 5 hours which having a difference of one hour, the addition of deposits increased significantly by 46.15% (0.6 g).

In the Ni synthesis process, it can be concluded that the greater the current and the holding time of the EDP process, the greater the weight of the Ni precipitation obtained, as shown by the graph of current flow and the duration of the EDP process against the weight of the metal precipitation (actual weight) obtained.

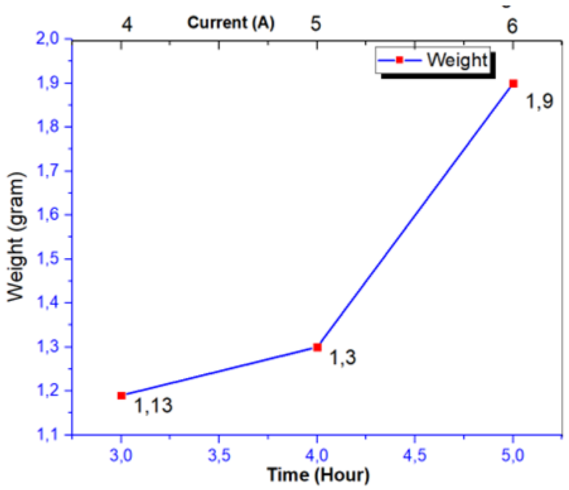

Figure 2. The effect of time on the processed weight of the deposit (actual weight)

Meanwhile, based on equation (1), the theoretical weight indicates that nickel with a process time variation of 3, 4, and 5 hours yields nickel weights of 13.14, 21.90, and 32.85 g, respectively. This is based on Faraday's first law of electrolysis. This law states that the magnitude of chemical changes (mass of substances deposited or dissolved) is directly proportional to the magnitude of electricity (charge) flowing through the electrolyte [16].

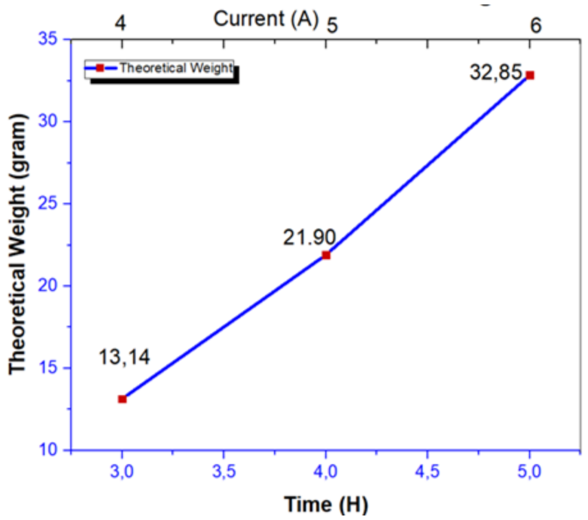

Figure 3. The effect of time and current on the theoretical weight of the deposit

Based on equation 1 for theoretical calculation of Ni electrodeposition process with time (t) = 3 hours (10800 s), current (I) = 4 A, molar (M) Ni = 58.69 g/mol, n is Ni's valence = 2, and F is the Faraday constant = 96.485 C/mol. Accordingly, the nickel (Ni) mass deposited during the three-hour EDP operation at 4 A is approximately 13.14 g. The weight of Ni obtained at times (t) 4 and 5 and current (5 and 6 A) is 21.90 and 32.85 g, respectively. Figure 3 shows the results of theoretical calculations. The results of theoretical calculations show that the addition of deposits increased by 66.67% (8.76 g) at a holding time of 3 to 4 hours, while at a holding time of 3 to 5 hours, it reached 150% (19.71 g).

The weight of Ni deposits produced by the EDP process for the 3 samples is smaller than their theoretical weight. The actual weight of the EDP process of 3 samples only reaches <3 g of nickel. Based on the theoretical weight, it reaches > 8 g, as shown in Fig. 4. In an electrolysis system using Nickel sulfate hexahydrate ($NiSO_4 \cdot 6H_2O$) in hydrochloric acid (HCl) as the electrolyte, the deposition of nickel (Ni) at the electrode follows Faraday's laws of electrolysis (equation 1), meaning that more current and longer time will lead to more nickel being deposited.

The solubility limit and other practical constraints inherent in this electrolyte system refer to the maximum concentration of $NiSO_4 \cdot 6H_2O$ that can be dissolved in solution. Once the solution becomes saturated with nickel sulfate, no additional nickel sulfate can be dissolved unless the temperature is raised or the solubility of the solution is changed. Suppose the concentration of Ni^{2+} ions drops below a certain level (due to electrolysis or limited solubility). In that case, the deposition rate will slow and eventually stop when insufficient ions are in the solution to precipitate on the electrodes [16]-[17].

The difference can be caused by a variety of factors, including the fact that the electrodeposition results do not adhere perfectly; this is also caused when removing (grinding) the nickel deposition; sanding must be done so that some of the nickel deposition is eroded, reducing the weight of the nickel deposition attached to the cathode. The pretreatment of the substrate surface before electroplating can have an impact on the adherence and homogeneity of the deposited nickel layer. Surface cleanliness, roughness, and the activation process. Furthermore, the electrochemical reactions involved in nickel electrodeposition are complex and controlled by variables such as overpotential, ion concentration gradients near the surface, and competition between hydrogen evolution and nickel deposition events. This will result in non-uniformity or divergence from the desired weight of nickel deposition as determined by theoretical data. The distribution of current density on the substrate surface might vary due to geometric factors such as substrate shape, proximity to the anode, and so on, which can cause the thickness or deposition of the deposited nickel layer to be non-uniform.

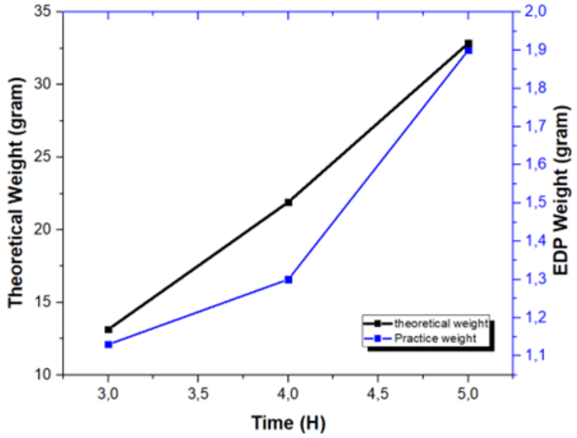

Figure 4. Weight comparison of Ni-EDP results processed with the theoretical weight

Because the electrodeposition process consumes current, the length of the process time influences the current efficiency. For example, sample 1, with a current of 4 A and a time of 3 hours, has a current efficiency of 9.01%, while sample 2, with a current of 5 A and a time of 4 hours, has a current efficiency of 5.9%. Sample 3, with a current of 6 A and a processing time of 5 hours, has a current efficiency of 6.9%, as shown in Fig. 5.

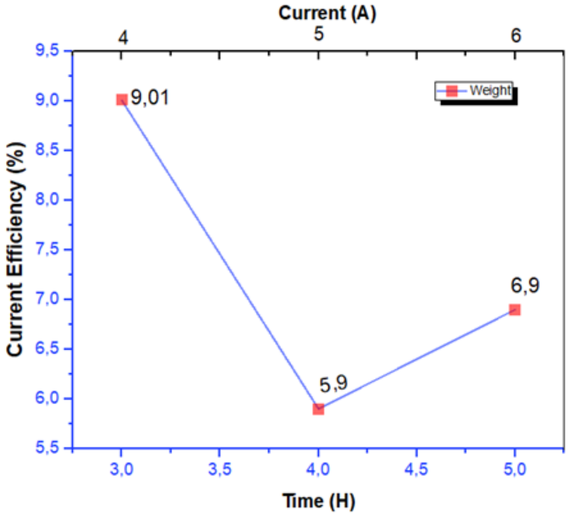

Figure 5. The effect of time on current efficiency

Current efficiency is related to the ratio of theoretical weight to actual weight. If the real weight approaches the theoretical weight, it generates a high percentage of current efficiency, and vice versa. If the actual weight deviates from the theoretical weight, the percentage of efficiency will decrease. The Optimal EDP process can cause variation of current efficiency during nickel EDP with different holding times of 3 hours. The conditions (e.g., nickel ion concentration, temperature, pH, current) are likely optimal, resulting in higher efficiency due to balanced ion availability and minimal side reactions [17]. During the 4-hour EDP process, Depletion and Increased Side Reactions occur; after 4 hours, the electrolyte may be depleted of nickel ions, and side reactions such as hydrogen evolution may increase, reducing the current efficiency. While at 5 hours of re-stabilization here, a new equilibrium may be reached, with some replenishment or redistribution of ions and reduced side reactions compared to 4 hours, leading to a slight increase in efficiency. The changes in efficiency are due to dynamic changes in electrolyte composition, surface conditions, and side reactions over time.

3.1 Visual Inspection

The visual inspection aimed to identify the color and appearance of nickel deposits formed during the electrodeposition process.

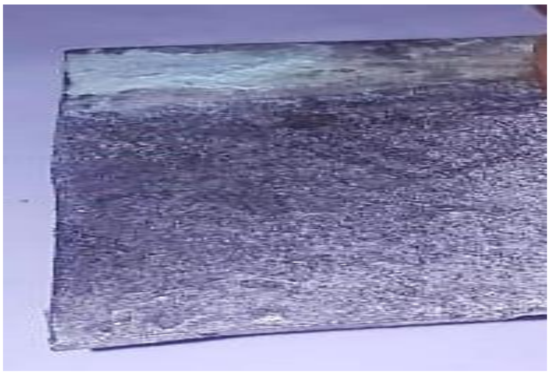

Figure 6. Visual appearance of nickel deposits attached to the cathode

The results of the Ni electrodeposition method with cornstarch additives yield porous nickel deposits linked to the cathode (ST-37 steel), as illustrated in Fig. 6.

Figure 7. Visual appearance of nickel deposits after being removed from the cathode

The electrodeposition method produces a thin layer. This layer has been peeled off the cathode and cured; it appears polished and has no color change, as shown in Fig. 7. However, the peeling thin layer only comprised a small portion of the existing cross-sectional area because the nickel deposits adhering to the cathode were not precisely even. Because the electrodeposition process time was less than ideal, the thickness of each surface of the nickel deposit was not uniform. The strength of the resulting nickel deposit layer varied depending on its thickness.

3.3 XRD Results

This XRD (x-ray diffraction) test detects the phase and compound generated during the Ni electrodeposition process, which uses $NiSO_4.6H_2O$ electrolyte solution [6]. Figure 8 shows the XRD test results, which identified phases such as α-Ni (81%), Ɣ-Fe (0.6%), and the compound produced Fe_1Ni_3 (18.5%).

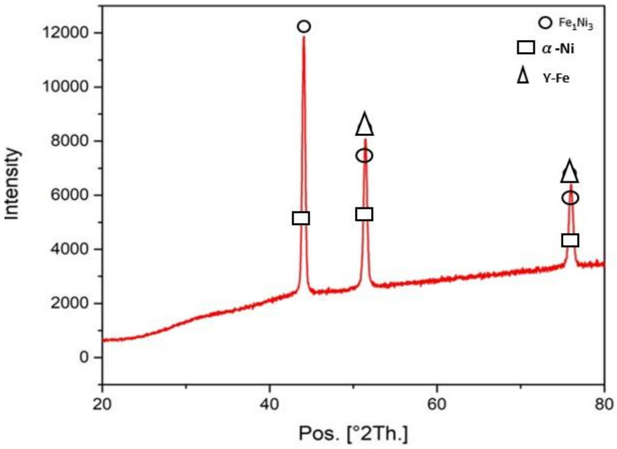

Figure 8. XRD results of nickel (electrodeposition)

3.4 SEM Results

The goal of SEM testing is to observe the electrodeposition process's results as well as the shape of the pores created by the operation. SEM testing findings are utilized to determine the size of pores generated during the electrodeposition process.

Based on the results of SEM (scanning electron microscopy) data characterization with a magnification of 500x on the test sample of the EDP process for 3 hours and a current of 4 A using 1 g of additive (corn starch), the surface morphology shows that there were two pores formed with a fairly large distance between them and their distribution was uneven, indicating that the pores formed did not reach the mesoporous size, as shown in Fig. 9. To demonstrate this, magnification was increased to 3000x, resulting in pores estimated to be ±10µm in diameter, as seen in Fig. 10.

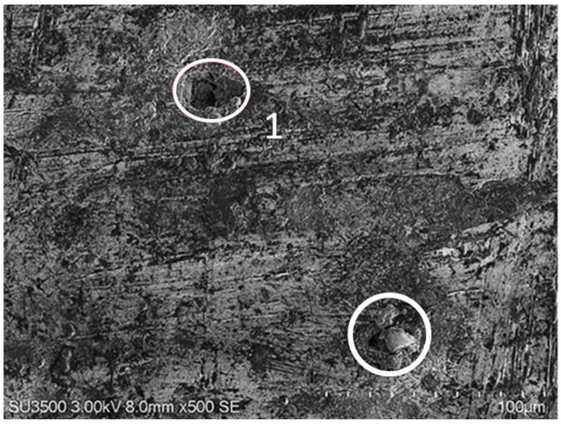

Figure 9. SEM results for mesoporous Ni for 3 hours, 4 A current, and 1 g of corn starch

SEM characterization results of EDP process samples using current I = 5 A, time t = 4 hours, and cornstarch weight of 2 g with a magnification of 2000x identified the presence of pores that began to spread evenly on each surface.

Figure 10. SEM results show that the porous size is estimated at 10 micrometers

Pore measurements were carried out at three points to obtain the diameters 1.09 µm, 689 nm, and 527 nm, as shown in Fig. 11.

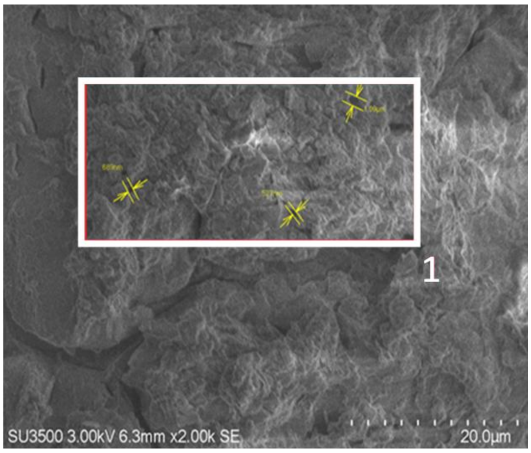

Figure 11. SEM test results of Mesoporous Ni for 4 hours, 5 A current, and 2 g of corn starch

The smallest pore size (527 nm) was found from three sites in these samples, indicating that the pore size created by this EDP technique is less than 600 nm. After performing a 3000x magnification, the surface morphology of the shaft size revealed several smaller shafts than before. Three points of the shaft size were taken, approximately in diameter 1.05 µm, 725 nm, and 516 nm. The smallest shaft size taken from the three different points was 516 nm in diameter. All the porous sizes obtained were almost evenly distributed between the two magnifications.

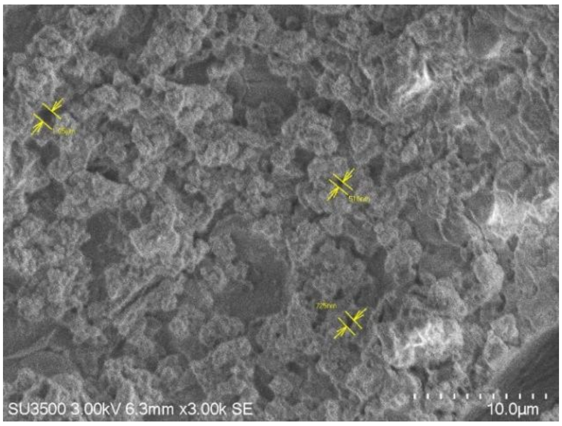

Figure 12. SEM test results on EDP process samples for 4 hours, 5 A current, and 2 g of corn starch, porous size is almost even

Figures 11 and 12 show the results of SEM testing, which used porous measurements to evaluate data distribution and how close the data was to the mean value, and the standard deviation or data deviation. The porosity generated at 2000x magnification was 1090 nm, 689 nm, and 527 nm, with a standard deviation of 289.83 nm and a mean of 768.67 nm. The standard deviation value is smaller than the average value (mean) of the results of measurements with 2000x and 3000x magnification, which indicates that the data is less varied using the data sufficiency test where the data confidence level is 90% with an error rate of 10% (0.1) requiring data from 16 test points. Due to testing limitations, the data confidence level is reduced to 80-90%, with an error rate of 20% (0.2). Consequently, the data sufficiency test requires 5.33 or 6 test points, given the almost homogeneous pore sizes.

At 3000x magnification, the pore sizes of 1050 nm, 725 nm, and 516 nm have a standard deviation of 269.09 nm and an average of 763.67 nm. The standard deviation value is smaller than the average value (mean) of the measurement results at 3000x magnification, this indicates that the data is less varied and the data confidence level ranges from 80-90% with an error rate of 20% (0.2) where the data adequacy test becomes 4.64 or at least there are 5 test points, with almost even and homogeneous pore sizes.

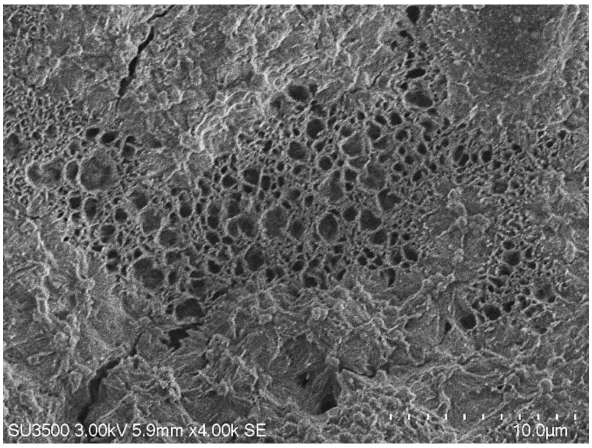

Figure 13. SEM test results of Mesoporous Ni for 5 hours, current of 6 A, and corn-starch weight of 3 g

SEM characterization results of samples with an EDP process duration of 5 hours, a current of 6 A, and a corn starch weight of 3 g at a magnification of 4000x revealed the presence of pores on all surfaces. The porous diameter was around 200 nm, and the space between pores was extremely tight, as illustrated in Fig. 13. A larger magnification was applied to the test sample, specifically 5000x. It was determined by the surface morphology of the porous size obtained at three sites along the porous diameter size, namely 195 nm, 170 nm, and 112 nm. According to the comparison of the three spots, the smallest porous size was 112 nm in diameter, as illustrated in Fig. 14.

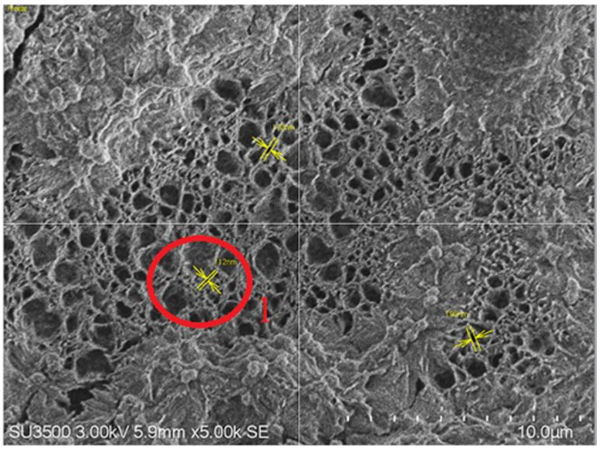

Figure 14. SEM test results for the sample with an EDP process time of 5 hours, current of 6 A, and cornstarch weight of 3 g show the shape of the shaft with a mesoporous size with a diameter of 112 nm

Based on SEM data, it can be observed that adding a substance, specifically corn starch, to a 1 M $NiSO_4 \cdot 6H_2O$ solution can produce pores in a thin layer of nickel deposits. The higher the content of corn starch given, the more pores are formed and distributed. However, this study is currently being conducted to determine the limits of corn starch addition, as excessive amounts of corn starch can increase oligomerization (clumping), rendering the electrodeposition process less than ideal.

3.5 EDS Results

Based on the data obtained from the EDS (energy dispersive spectroscopy) characterization of samples with variations of I = 4 A, t = 3 hours, with the addition of corn starch additives = 1 gram, testing in selected area 1, the composition of the identified elements was Ni, Fe, P, and Cl, with levels of 81.96 wt.%-Ni and 6.52 wt.%-Fe, the remaining of 0.83 wt.%-Cl and 1.86 wt.%-P, shown in Fig. 15 and Table 1.

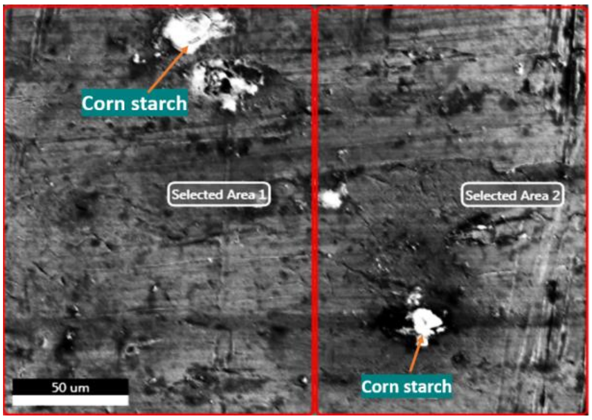

Figure 15. Selected area SEM EDS selected area 1 & selected area 2

While in selected area 2, the composition of the elements was 85.35 wt.% Ni, the second position is Cl of 6.86 wt.%, At the same time, Fe ranked third at 6.52 wt.%, with P at 0.79 wt.%, as shown in Fig. 15 and Table 2.

Table 1. EDS test results selected area 1

Element	EDS Test Selected Area 1	
	Weigth%	Atomic%
FeL	7.63	6.51
NiL	81.96	66.53
ClK	1.86	2.86
PK	0.83	1.12

The EDS measurements reveal that the nickel EDP procedure was successful, as the Ni deposit on the workpiece's surface exceeded 80%.

Table 2. EDS test results selected area 2

Element	EDS Test Selected Area 2	
	Weigth%	Atomic%
FeL	6.52	5.73
NiL	85.35	71.32
ClK	6.86	21.04
PK	0.79	1.25

Ni concentration on the surface of ST 37 steel exceeds 80 wt%. The EDS test results show a low P content (<1% wt%) in areas 1 and 2. This is due to the cornstarch additive that was left behind/attached to the Ni deposit, as evidenced by the SEM test results in Fig. 15. The presence of Cl (Chloride) comes from the HCl electrolyte solution used in the EDS process, which was left behind and attached to the Ni deposit. The BCPS, ESC, MMBPs, LLC, and EDP are examples of current approaches used in mesopore research [12]-[18]. The EDP process carried out by previous researchers used ethanol, alkali, and polymer catalysts [12]-[19]. In contrast, the new thing about this EDP process is cornstarch as a catalyst/additive that creates porous materials.

4. CONCLUSION

The electrodeposition process showed that the amount of nickel (Ni) deposited increased with higher electric current and longer processing time, with the lowest deposition of 1.19 g occurring at 4 A and 3 hours, increasing to 1.3 g at 5 A and 4 hours, and reaching the highest at 1.9 g with 6 A and 5 hours. SEM (scanning electron microscope) analysis revealed that the largest pore diameter, 1090 nm, was found in sample 1, which used a current of 4 A, a duration of 3 hours, and an addition of 1 gram of corn starch, while the smallest pore diameter of 112 nm was observed in sample 3 (6 A, 5 hours), with an average pore size of approximately 200 nm and closely packed structures. These findings suggest that increasing the concentration of corn starch leads to more porous and evenly distributed deposits. Furthermore, XRD (x-ray diffraction) analysis identified the presence of α-Ni, ϒ-Fe, and Fe_1Ni_3 phases, and combined XRD and SEM-EDS results confirmed the formation of porous nickel deposits with a nickel content exceeding 80%.

ACKNOWLEDGMENT

The author wishes to thank PRTPR BRIN for supplying materials, tools, and research sites, as well as Metallurgical Engineering FTM-UNJANI and all others who assisted the author in carrying out this research.

REFERENCES

[1] S. Polarz and B. Smarsly, “Nanoporous materials,” *J Nanosci Nanotechnol*, vol. 6, pp. 581-612, 2002. DOI: 10.1166/153348802321105860.

[2] Y. D. Gamburg, G. Zangari, “*Theory and practice of metal electrodeposition*,” Springer, pp. 292-295, 2011. DOI: 10.1007/978-1-4419-9669-5

[3] X. Pu, W. Zhang, M. Ma, D. Shi, S. Han, L. Xiong, “Atomic nickel on controllable

mesoporous carbon nanospheres to boost electrochemical carbon dioxide reduction," *International Journal of Ionics The Science and Technology of Ionic Motion,* vol. 29, pp. 3683-3692, 2023. DOI:10.1007/s11581-023-05095-8.

[4] T. Kouznetsova, A. Ivanets, V. Prozorovich, P. Shornikova, L. Kapysh, Q. Tian, L. Péter, L. Trif, and L. Almásy, "Design of nickel-containing nanocomposites based on ordered mesoporous silica: synthesis, structure, and methylene blue adsorption," *MDPI Journal*, vol. 10, no. 2, p.133, 2024. DOI:10.3390/gels10020133.

[5] L. Hao and B. Liu, "Two-dimensional mesoporous metals: a new era for designing functional electrocatalysts," *Royal Society of Chemistry, Chemical Science,* vol. 14, p. 13313, 2024. DOI: 10.1039/d3sc04244h.

[6] W. Liu, M. Luo, F. Luo, Y. Liu, Y. Zhang, F. Shen, X. Zhang, G. Yang, L. Wang, S. Deng, "Three-dimensional Cu-Ni composite superamphiphobic surface via electrodeposition and fluoro silane," *Chinese Journal of Chemical Physics,* vol. 33, pp. 343-348, 2020. DOI:10.1063/16740068/cjcp1905109.

[7] F. Nasirpouri, "Electrodeposition of nanostructured materials," *Springer Series in Surface Sciences*, vol. 62, pp.1-32, 2017. DOI:10.1007/978-3-319-44920-3.

[8] A. El-Zoka, A. G. Carcea, M. Ghaznavi, R. C. Newman, "Electrodeposition of metals and metal oxides into nanoporous gold," *ECS The Electrochemical Society*, vol. 2, no. 16, pp 904-904, 2017. DOI: 10.1149/MA2017-02/16/904.

[9] M. Miyake, A. Takahashi, T. Ikenoue, T. Hirato, "Fabrication of photocatalytic Al-TiO_2 coatings by composite electrodeposition and anodization," *ECS The Electrochemical Society,* vol. 01, no. 21, 2016. DOI: 10.1149/MA2016-01/21/1129.

[10] E. Juzeliunas, "Silicon electrowinning and electrodeposition of thin layers," *Silicon*, pp. 49-76, 2022. DOI:10.1002/9783527831913.ch6.

[11] R. A. Karim, Y. Reda, K. M. Zohdy, A. Abdelfatah, S. El-Raghy, "Electrochemical performance of porous Ni-Cu anodes for direct methanol fuel cells," *International Journal of Electrochemical Science*, vol. 13, no. 3, 2019. DOI:10.20964/2019.03.59.

[12] J. Zhang, M. D. Baro, E. Pellicer and J. Sort, "Electrodeposition of magnetic, superhydrophobic, non-stick, two-phase Cu-Ni foam films and their enhanced performance for hydrogen evolution reaction in alkaline water media," *Nanoscale,* vol. 6, no. 21, pp. 12490-12499, 2014. DOI:10.1039/c4nr03200d.

[13] M. Faraday, "Experimental researches In electricity. Series VII (1834), On the absolute quantity of electricity associated with the decomposition of electrolytes," *Project Gutenberg,* vol. 124, pp. 84-94, 2005. DOI:10.1098/rstl.1834.0008.

[14] A. A. Bunaciu, E. G. Udriştioiu, and H. Y. A. Enein, "X-ray diffraction: instrumentation and applications," *Crit. Rev. anal. Chem.*, vol. 45, no. 4, pp. 289-299, 2015. DOI:10.1080/10408347.2014.949616.

[15] S. M. Janjan, F. Nasirpouri, M. G. Hosseini, "Electrodeposition mechanism of nickel films on polycrystalline copper from dilute simple sulphate solutions," *Russian Journal of Electrochemistry*, vol. 47, no. 7, pp 787-792, 2011. DOI:10.1134/S1023193511070159.

[16] F. Nasirpouri, S. M. Jajan, S. M. P. Sattari, M. G. Hosseini, A. Akbari, A. S. Samardak, "Refinement of electrodeposition mechanism for fabrication of thin nickel films on n-type silicon (111)," *Journal of Electroanalytical Chemistry*, vol. 690, no. 136, 2012. DOI: 10.1016/j.jelechem.2012.07. 005.

[17] Shobit, S. Ritu and B. S. Khatkar, "Assessment of physicochemical properties of popular brands of corn starch for custard Preparation," *International Journal of Chemical Studies*, vol. 8, no. 4, 3631-3637, 2020. DOI: 10.22271/chemi2020.v8.i4at 10211.

[18] Y. Zou, X. Zhou, J. Ma, X. Yang and Y. Deng, "Recent advances in amphiphilic block copolymer templated mesoporous metal-based materials: assembly engineering and applications," *Chem. Soc. Rev.*, vol. 49, pp. 1173-1208, 2020. DOI:10.1039/C9CS00334G.

[19] M. A. Ghanem, A. M. Mayouf, J. P. Singh, T. Abiti, and F. Marken "Mesoporous nickel/nickel hydroxide catalyst using liquid crystal template for ethanol oxidation in alkaline solution," *Journal of*

The Electrochemical Society, vol. 162, no. 7, pp. 453-459, 2015. DOI: 10.1149/2.0441507jes.

Metalurgi (2024) 2:73 - 78

METALURGI
Majalah Ilmu dan Teknologi
p-ISSN 0126-3188 | e-ISSN 2443-3926
ejurnalmaterialmetalurgi.lipi.go.id

STUDY OF IRON AND CALCIUM REMOVAL ON MANGANESE SULFATE PRECURSORS FOR BATTERY CATHODE RAW MATERIAL APPLICATIONS

Agsel Fauzia Hakim[a,*], Lia Andriyah[b,c], Soesaptri Oediyani[a], Latifa Hanum Lalasari[b], Eko Sulistiyono[b], Januar Irawan[b], Tri Arini[b,c], Fariza Eka Yunita[b], Ariyo Suharyanto[b], Iwan Setiawan[b], Florentinus Firdiyono[b], Akhmad Herman Yuwono[c,d]

[a]Department of Metallurgy, Sultan Ageng Tirtayasa University
Jl. Jenderal Sudirman Km 3, Cilegon, Banten, Indonesia 42435
[b]Research Center for Metallurgy, National Research and Innovation Agency (BRIN)
B.J. Habibie Sains and Technology Area, Banten, Indonesia 15314
[c]Department of Metallurgical and Materials Engineering, University of Indonesia
[d]Advanced Materials Research Center, University of Indonesia
Kampus UI, Kukusan, Depok, Indonesia 16424
*E-mail: agselfauzia11@gmail.com

Received: 21-05-2024, Revised: 02-01-2025, Accepted: 10-01-2025

Abstract

Global battery sales are expected to reach $310.8 billion in 2027, up 14.1% from 2020. 95% of the world's batteries are lead-acid, lithium-ion, or nickel-based. One of the most popular batteries on the global market is lithium-ion, which uses MnSO4 powder as its cathode raw material. Manganese sulfate-based lithium-ion batteries can be made using Indonesian resources, specifically manganese ore from Trenggalek. Trenggalek manganese ore is of poor quality and contains impurities, primarily Fe and Ca. To produce 98% powder manganese sulfate, the solution is prepared, reduced with briquette charcoal, leached, precipitated, carbonated, and crystallised. NH_4OH reagent is used to remove Fe through precipitation, and the carbonatation process is employed to eliminate Ca, resulting in 97.237% purity of manganese sulfate powder product. This outcome is achieved under precipitation process conditions of [NH_4OH 2M], T = 80 °C, pH = 4, t =180 minutes, while carbonatation process conditions are T=50 °C, t = 120 minutes.

Keywords: *Lithium-ion batteries, iron recipitation, carbonatation, manganese sulphate*

1. INTRODUCTION

Batteries are the technology used for energy storage. Climate change is transitioning from fossil fuels to sustainable energy solutions, including batteries and bioenergy [1]. Analysis by the McKinsey Battery Insights team projects that the entire lithium-ion (Li-ion) battery chain, from mining through recycling, could grow by over 30 percent annually from 2022 to 2030. Batteries for mobility applications, such as EVs (electric vehicles), will account for the vast bulk of demand in 2030, about 4,300 GWh, an unsurprising trend, seeing that mobility is growing rapidly. This is largely driven by three major drivers: a regulatory shift toward sustainability, increased consumer demand for greener technologies, and emission-reduction targets [2].

With its potential in Indonesia, manganese sulfate powder can be utilized as a raw material for lithium-ion battery cathodes. Manganese sulfate powder is considered more efficient than

DOI : 10.55981/metalurgi.2024.753

Metalurgi is Sinta 2 Journal (https://sinta.kemdikbud.go.id/journals/profile/3708) accredited by Ministry of Education, Culture, Research, and Technology, Republic Indonesia

manganese dioxide as a raw material for cathodes because the cations in the produced powder can store energy in the battery, resulting in better battery life than manganese dioxide as a cathode material [3]. The increasing global demand for manganese from many sectors that use manganese as a primary or supporting material for a product has led to very rapid and varied production of manganese [4].

The potential of manganese ore in Indonesia can be maximized as raw material for lithium-ion battery cathodes to fill the global battery market, which is one of the contributions in this era. The world's total reserves amount to 1.3 billion tons, and Indonesia's manganese ore reserves are 49.6 million tons according to the OEC (observatory of economic complexity). Although it only has a small portion of manganese reserves, its quality ranks as the best number one in the world. Manganese ore is an important mineral used as a raw material or alloying element in the manufacturing process of various products, including manganese as a raw material for lithium battery cathodes. In Trenggalek manganese ore, there are several main impurities, such as Ca and Fe, which pose a problem because the desired product for manganese sulfate powder production requires a purity of 98%, according to ISO 9001 and SNI 23625:2021 standards.

To obtain $MnSO_4$ from Trenggalek manganese ore, the process begins with leaching the Mn ore using H_2SO_4, followed by precipitation and carbonation, each intended to remove Fe and Ca, respectively. In the iron precipitation process in this study, the NH_4OH reagent is used, which is known to easily precipitate iron and other elements, with less than 5% [5]. The reactions occurring during the Fe precipitation process are explained in equations 1-3 [6][7][8].

$$\mathrm{MnO\ (s) + H_2SO_4\ (aq) \rightarrow MnSO_4\ (aq) + H_2O\ (aq)} \quad \ldots\ldots(1)$$

$$\mathrm{MnSO_4\ (aq) + \mathbf{2}\ NH_4OH\ (aq) \rightarrow Mn(OH)_2\ (s) + (NH_4)_2SO_4\ (aq)} \quad \ldots\ldots(2)$$

$$\mathrm{FeSO_4\ (aq) + 2\ NH_4OH\ (aq) \rightarrow Fe(OH)_2\ (s) + (NH_4)_2SO_4\ (aq)} \quad \ldots\ldots(3)$$

A carbonatation process is carried out during the precipitation or removal of Ca. The result of the Ca precipitate obtained from carbonatation is $CaCO_3$. The carbonatation process is a solution saturation process by flowing CO_2 gas into the solution at a certain temperature and a fixed discharge [9]. The reaction will occur when the carbonatation process is carried out [10]-[12].

$$\mathrm{CO_2(g) + H_2O(l) \rightarrow H_2CO_3(aq)} \quad \ldots\ldots(4)$$

$$\mathrm{H_2CO_3(aq) \rightleftharpoons H+(aq) + HCO_3\text{-}(aq)} \quad \ldots\ldots(5)$$

$$\mathrm{H^+(aq) + HCO_3^-(aq) \rightleftharpoons 2H^+(aq) + CO_3^{2-}\ (aq)} \quad \ldots(6)$$

$$\mathrm{Ca^{2+}(aq) + 2OH^-(aq) + 2H^+(aq) + CO_3^{2-}(aq) \rightarrow CaCO_3(s) + 2H_2O(l)} \quad \ldots\ldots(7)$$

2. MATERIALS AND METHODS

Manganese ore was ground into a size of -80# +100# and then mixed with briquette charcoal of the same size, which is used as a reducer. The ratio between manganese ore and briquette charcoal is 4:1. It was then calcined at a temperature of 800 °C in a muffle furnace for 2 hours. The resulting calcination product is then quenched. Next, a leaching process is conducted to extract manganese ore using 4M H_2SO_4 at 70 °C for 1.5 hours. The precipitation process to remove Fe is carried out using 4M NH_4OH at 80 °C with variations in pH and time on the pregnant leach solution. The best precipitation result undergoes a process of removing Ca by carbonatation using CO_2 gas passed through the solution with variations in temperature and time. The solution then crystallized to convert into manganese sulfate powder.

3. RESULTS AND DISCUSSION

The results of XRF (x-ray fluorescence) analysis of Trenggalek manganese ore samples can be seen in Table 1.

Table 1. XRF analysis of manganese ore from Trenggalek

Element	Compound	Wt.%
Ca	CaO	36,50
Mn	MnO_2	33,10
Si	SiO_2	1,20
Fe	Fe_2O_3	0,80
Mg	MgO	0,10
Al	Al_2O_3	0,40
More	...	27,9

Table 1 shows that many other impurities are still found in Trenggalek manganese ore, even if the impurity content exceeds the Mn element.

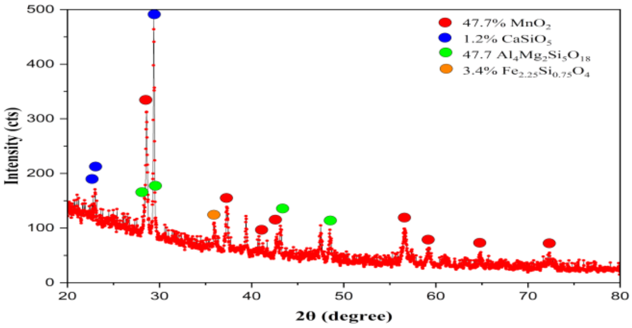

Figure 1. XRD analysis for manganese ore

With less than 35%, Manganese ore is categorized as low-grade manganese ore. Figure 1 presents the XRD (x-ray diffraction) analysis for the manganese ore. The XRD analysis in Fig. 1 was performed in the 20-80º range. Four compounds were identified: MnO_2, $CaSiO_5$, $Al_4Mg_2Si_5O_{18}$, and $Fe_2.25Si0.75O_4$. The main compound detected is MnO_2, with an intensity of 47.7% in the XRD analysis. MnO_2 is scattered at several points or peaks in the XRD analysis results. MnO_2 is the primary compound to be processed in producing manganese sulfate ($MnSO_4$) precursor as a raw material for lithium battery cathodes.

The briquette charcoal used as a reductant in this research was analyzed proximate using ASTM D3172 - ASTM D3175 standards. Table 2 presents the proximate analysis for the charcoal briquettes used in this study.

Table 2. Proximate analysis for charcoal briquettes

Parameter	**Test results (%)**
Moisture	19
Volatile Matter	5
Ash	41
Fixed Carbon	35

In addition to the charcoal briquettes, the composition of the manganese ore reduction was analyzed using XRF, as shown in Table 3.

Table 3. XRF analysis for the composition of manganese ore reduction

Element	**Compound**	**Wt.%**
Ca	CaO	53.06
Mn	MnO_2	36.74
Si	SiO_2	7.41
Sn	SnO_2	0.05
More		2.74

As in Table 3**,** the concentration of CaO reaches a peak of 53.06%**,** which indicates the CaO-rich phase as a matrix constituent. All the remaining elements were purified and removed as the samples were carried out for refining. These processes increased the purity of Mn from 33.1% to 36.74% and Ca from 36.5% to 53.06%. Briquette charcoal can be used as a reducer because it can convert the valence state of Mn^{4+} to Mn^{2+}, as Mn^{2+} is more readily leached by acid than Mn^{4+}. Using briquette charcoal as a reducing agent causes the conversion of Mn^{4+} to Mn^{2+} and increases the manganese ore content.

The leaching process of manganese ore is carried out under acidic conditions using sulfuric acid (H_2SO_4) at a concentration of 4 M at 70 °C for 90 minutes with a stirring speed of 350 rpm. Table 5 shows the results of the ICP-OES (inductively coupled plasma-optical emission spectroscopy) analysis of the manganese ore leaching with a 10x dilution.

Table 4 shows that the Mn content in the PLS (pregnant leach solution) increases after the leaching process up to 17777 ppm.

Table 4. ICP-OES analysis for pregnant leach solution

Element	**ppm**	**Element**	**ppm**
Mn	17777	Na	204
Al	1662	K	101
Fe	743	Ti	49
Mg	286	Sn	46
Ca	220	Si	40

Precipitation is carried out on a 20 mL filtrate of the PLS by adding reagent [NH_4OH 2M] at a temperature of 70 °C with variations in pH and time. The pH variations used are 4, 6, 8, 10, and 12, while the time variations used are 60 minutes, 120 minutes, and 180 minutes. The percentage removal of Fe is obtained from the following formula.

$$Removal\ (\%) = \frac{Initial\ Element\ Level\ (ppm) - Final\ Element\ Level\ (ppm)}{Initial\ Element\ Level\ (ppm)} x100$$

This formula quantifies the efficiency of Fe removal under different conditions.

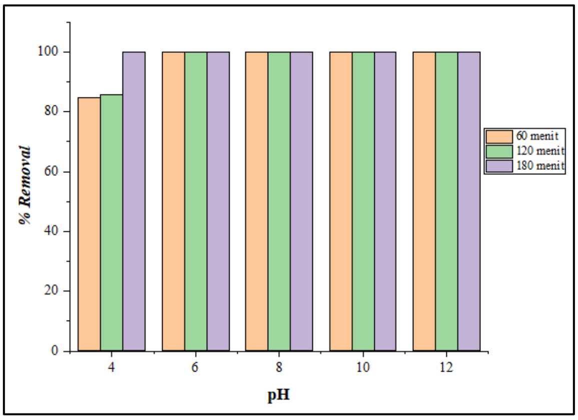

Figure 2. Effect of pH variations on percent Fe removal

Figure 2 illustrates the effect of pH variations on the percentage of Fe removal.

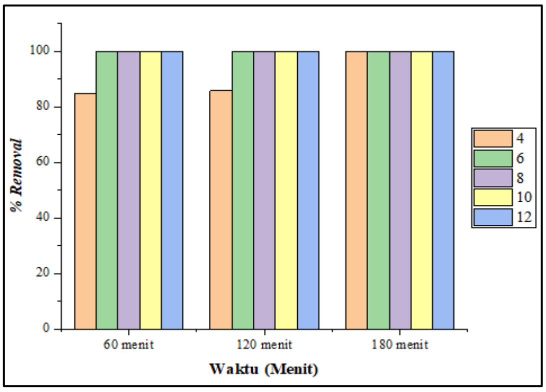

Figure 3. Effect of time variations on percent Fe removal

The higher the pH, the greater the Fe that can be removed. This happens because Fe can precipitate in the pH range of 1 - 2.5, producing Fe^{3+} ion precipitates, while in the pH range of 6.5 - 8.5, producing F^{2+} ion precipitates, referring to the Monhemius diagram [13]. The smaller the concentration of Fe^{3+} ions, the higher concentration of OH^- ions is needed, and increasing the concentration of OH^- can be done by increasing the pH of the solution [14]. To further investigate the influence of other variables, Fig. 3 illustrates the effect of time variations on the percentage of Fe removal. The highest condition in the Fe precipitation process is at pH 4, with a precipitation process of 180 minutes, which is 100%, with the remaining Mn content in the filtrate of 6.129 ppm, the highest level compared to other variable conditions. The time used affects the maximum precipitate results because the time used in the precipitation process can cause the process to occur optimally between the PLS sample and the precipitation agent, namely NH_4OH [15].

Table 5. ICP-OES analysis for the filtrate before and after the Fe precipitation

Element	Before the precipitation process of Fe (ppm)	After the precipitation process of Fe (ppm)
Al	1.662	209
Ca	220	117
Fe	743	0
K	101	19.3
Mg	286	20
Mg	286	20
Mn	17.777	6.13
Na	204	38.2
Si	40	35.7
Sn	46	28.3

Table 5 shows that several elements are missing in the filtrate that precipitate in the residue during the Fe precipitation process using NH_4OH. This occurs because using NH_4OH as a precipitation reagent is not selective in precipitating Fe. The carbonatation process was carried out by flowing CO_2 gas with a discharge of 5 L/min to the best filtrate sample of Fe precipitation results using NH_4OH as much as 100 mL with an agitation speed of 200 rpm. Time variations are 40 minutes, 80 minutes, and 120 minutes. At the same time, the temperature variations are 30, 40, and 50 °C. As shown in Fig. 4, the temperature used in the carbonatation process significantly affects the precipitation of Ca. The temperature used in the carbonatation process affects the precipitation of Ca. Figure 4 illustrates that the higher the temperature, the greater the percentage of Ca precipitation.

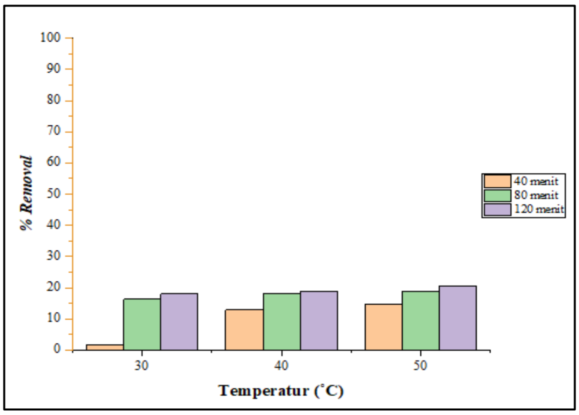

Figure 4. Effect of temperature on Ca precipitation

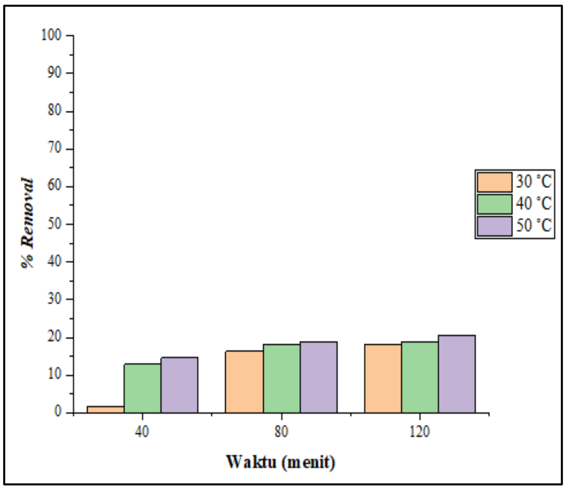

Figure 5. Effect of time on Ca precipitation

This is because, at higher temperatures, the reaction between calcium and CO_2 to form calcium carbonate occurs more easily[16]. In addition to temperature, Fig. 5 illustrates the effect of time on Ca precipitation.

(a) (b)

Figure 6. (a) Crystallization process, and (b) Product after crystallization

In this study, the longer the time used, the more Ca can be deposited; this happens because the CO_2 gas that reacts with the filtrate sample will form more calcium carbonate, and the longer the temperature used, the more calcium carbonate will be formed. The best conditions in this study were 120 minutes and 50 °C with 20.51% Ca precipitation [16]. Following the precipitation phase, the crystallization process is depicted in Fig. 6. Figure 6(a) shows the crystallization process, while Figure 6(b) presents the product after crystallization. Table 6 presents the XRF analysis for the manganese sulfate product. The composition details in this table highlight the significant elements and compounds present in the product.

Table 6. XRF analysis for manganese sulfate product

Element	Compound	Wt.%
S	SO_3	70.457
Mn	MnO	26.78
P	P_2O_5	0.823
Ca	CaO	0.683
Al	Al_2O_3	0.647
K	K_2O	0.361
Si	SiO_2	0.131
Cu	CuO	0.06
Ni	NiO	0.03
Zn	ZnO	0.0186
V	V_2O_5	0.0074
Br	Br	0.002
Total		100

The purity of the powdered manganese sulfate product is 97.237%. Typically, the usage requirement for powdered manganese sulfate as a raw material for lithium battery cathodes is 98%.

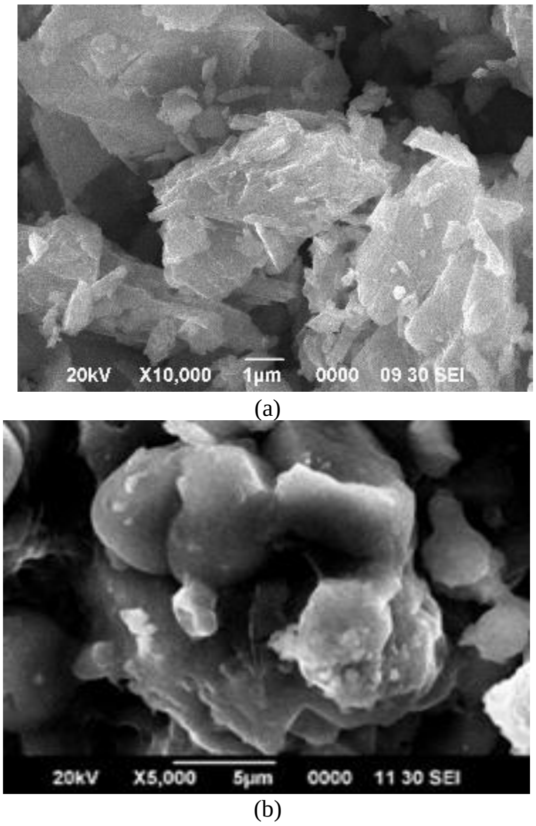

(a)

(b)

Figure 7. (a) SEM analysis of manganese ore, (b) SEM analysis of the manganese sulfate product

Figures 7(a) and 7(b) display the morphology of both the manganese ore and the manganese sulfate product. Figure 7(a) Trenggalek manganese ore is in the form of rough tetragonal crystals; this form (MnO_2 or pyrolusite) is caused by elements that form metallic gray manganese oxide compounds is the morphological form of manganese ore before a process is carried out. Meanwhile, Figure 7(b) is the morphology of the manganese sulfate powder product after undergoing several processes, where the surface is smoother than before the process.

4. CONCLUSION

The quality of manganese sulfate ($MnSO_4$) powder products is 97.237%. The optimal conditions for the Fe precipitation procedure employing the NH_4OH reagent are pH 4 for 180 minutes and 100% Fe elimination. The optimal temperature for Ca precipitation in carbonatation is 50 ºC for 120 minutes, resulting in a 20.51% Ca removal rate.

ACKNOWLEDGMENT

The authors would like to acknowledge PT. Timah, Tbk, for providing the necessary resources and support for this project.

REFERENCES

[1] E. Asadi Dalini, G. Karimi, S. Zandevakili, and M. Goodarzi, “A review on environmental, economic and hydrometallurgical processes of recycling spent lithium-ion batteries,” *Miner. Process. Extr. Metall. Rev.*, vol. 00, pp. 1-22, 2020. DOI: 10.1080/08827508.2020.1781628.

[2] J. Fleischmann, M. Hanicke, E. Horetsky, D. Ibrahim, S. Jautelat, and M. Linder, “Battery 2030: Resilient, sustainable, and circular,” *McKinsey & Company*, 2023. https://www.mckinsey.com/industries/automotive-and-assembly/our insights/battery-2030-resilient-sustainable-and-circula.

[3] Itsuna, “Utilization of lithium batteries in electric vehicles,” *ITS Online*. 2022, [Online]. Available: https://www.its.ac.id/news/2022/02/17/pemanfaatan-baterai-lithium-dalam-kendaraan-listrik/.

[4] A. E. Elsherief, “Study of the electroleaching of manganese ore,” *Hydrometallurgy*, vol. 55, no. 3, pp. 311-326, 2000. DOI: 10.1016/S0304-386X(99)00089-4.

[5] Y. Min and Y. S. Jun, “Wollastonite carbonation in water-bearing supercritical

CO_2: Effects of water saturation conditions, temperature, and pressure," *Chem. Geol.*, vol. 483, pp. 239-246, 2018. DOI: 10.1016/j.chemgeo.2018.01.012.

[6] M. Osali, F. Ahani, H. Khodaei, P. Mohammadi, J. Moghaddam, and S. Karimi, "Reductive leaching and recovery of nano-crystalline MnO_2 from low-grade pyrolusite ore," *Journal of Sustainable Metallurgy*, vol. 9, no. 3, pp. 1268-1278, 2023. DOI: 10.1007/s40831-023-00724-y.

[7] X. Cai, F. Shen, Y. Zhang, H. Hu, Z. Huang, Y. Yin, X. Liang, Y. Qin, and J. Liang, "Mineralization of organics in hazardous waste sulfuric acid by natural manganese oxide ore and a combined MnO_2/activated carbon treatment to produce qualified manganese sulfate," *J. Hazard. Mater.*, vol. 366, pp. 466-474, 2019. DOI: 10.1016/j.jhazmat.2018.12.021.

[8] D. Cornu, R. Coustel, P. Durand, C. Carteret, and C. Ruby, "How can pH drop while adding NaOH? Formation and transformation of $Mn_4(OH)_6SO_4$," *J. Solid State Chem.*, vol. 305, 2022. DOI: 10.1016/j.jssc.2021.122631.

[9] R. Kusumaningrum, S. A. Rahmani, W. B. Widayatno, A. S. Wismogroho, D. W. Nugroho, S. Maulana, N. T. Rochman, and M. I. Amal, "Characterization of Sumbawa manganese ore and recovery of manganese sulfate as leaching products," *AIP Conf. Proc. 1964*, 020042, 2021. DOI :10.1063/1.5038324

[10] V. Singh, T. Chakraborty, and S. K. Tripathy, "A review of low-grade manganese ore upgradation processes," *Miner. Process. Extr. Metall. Rev.*, vol. 41, no. 6, pp. 417-438, 2020. DOI: 10.1080/08827508.2019.1634567.

[11] M. A. Rashid, T. Acter, and N. Uddin, "The solvation dynamics of CO_2 by quantum mechanical molecular dynamics," *Chem. Phys. Lett.*, vol. 832, p. 140861, 2023. DOI: 10.1016/j.cplett.2023.140861.

[12] J. Conrad, S. Sasidharanpillai, and P. R. Tremaine, "Second dissociation constant of carbonic acid in H_2O and D_2O from 150 to 325 °C at p = 21 MPa using raman spectroscopy and a sapphire-windowed flow cell," *J. Phys. Chem. B*, vol. 124, no. 13, pp. 2600-2617, 2020. DOI: 10.1021/acs.jpcb.9b11358.

[13] A. Chernyaev, J. Zhang, S. Seisko, M. L. Kultanen, and M. Lundström, "$Fe3^+$ and $Al3^+$ removal by phosphate and hydroxide precipitation from synthetic NMC Li-ion battery leach solution," *Sci. Rep.*, vol. 13, no. 1, pp. 1-13, 2023. DOI: 10.1038/s41598-023-48247-6.

[14] B. Al-Harbi, N. Aljeaban, A. Graham, and K. Sorbie, "Critical review on sulphide scale formation, removal and inhibition," *NACE - Int. Corros. Conf. Ser.*, pp. 23-25, 2020.

[15] A. A. Nayl, I. M. Ismail, and H. F. Aly, "Recovery of pure $MnSO_4 \cdot H_2O$ by reductive leaching of manganese from pyrolusite ore by sulfuric acid and hydrogen peroxide," *International Journal of Mineral Processing*, vol. 100, no. 3-4. pp. 116-123, 2011. DOI: 10.1016/j.minpro.2011.05.003.

[16] W. J. J. Huijgen, G. J. Witkamp, and R. N. J. Comans, "Mechanisms of aqueous wollastonite carbonation as a possible CO_2 sequestration process," *Chem. Eng. Sci.*, vol. 61, no. 13, pp. 4242-4251, 2006. DOI: 10.1016/j.ces.2006.01.048.

Metalurgi (2024) 2: 79 - 88

BRIN
BADAN RISET
DAN INOVASI NASIONAL

METALURGI
Majalah Ilmu dan Teknologi
p-ISSN 0126-3188 | e-ISSN 2443-3926
ejurnalmaterialmetalurgi.lipi.go.id

OPTIMIZATION OF NMC811 SYNTHESIS VIA OXALATE COPRECIPITATION METHOD FOR LITHIUM-ION BATTERY CATHODE

Fiona Angellinnov[a], **Achmad Subhan**[b], **Bambang Priyono**[a,c], **Anne Zulfia Syahrial**[a,c,*]

[a]Department of Metallurgical and Materials Engineering, University of Indonesia
Kampus UI, Kukusan, Depok, Indonesia 16424
[b]Research Center for Advanced Materials, National Research and Innovation Agency (BRIN)
B.J. Habibie Sains and Technology Area, Banten, Indonesia 15314
[c]Tropical Renewable Energy Centre, University of Indonesia
Kampus UI, Kukusan, Depok, Indonesia 16424
*E-mail: anne.zulfia@ui.ac.id

Received: 30-08-2024, Revised: 14-10-2024, Accepted: 21-10-2024

Abstract

NMC811 was synthesized through the oxalate coprecipitation method, followed by the solid-state method of lithiation. Stirring speed (500, 750, 1000 rpm), aging time (0, 3, 5h), sintering atmosphere (with and without oxygen flow), sintering temperature (700, 750, 800 °C), and lithium concentration (0, 2, 5% excess) effect on the NMC811 were examined. Characterization results showed that the optimum stirring speed and aging time are 750 rpm and 3 hours. Based on structural analysis, the best condition for sintering is in oxygen atmospheres at 800 °C with a lithium concentration of 2% excess. NMC811, synthesized with these optimum parameters, provided a 212.93 mAh/g capacity. These findings deliver insight into NMC811 synthesis optimization.

Keywords: *Cathode material, oxalate coprecipitation, NMC811, synthesis method*

1. INTRODUCTION

Lithium-ion batteries are commonly used in portable electronic devices such as laptops, mobile phones, and electric vehicles [1]. The price and performance of a LIB are determined by its active cathode material [2]. Among the cathode materials, nickel manganese cobalt ($LiNi_xMn_yCo_zO_2$, NMC) is known to have high specific capacity and operational voltage [3]. Compared to the other types of NMC, NMC811 ($LiNi_{0.8}Mn_{0.1}Co_{0.1}O_2$) possesses the highest specific capacity of about ~160-200 mAh/g, whereas at the same time, it is cheaper due to its lower cobalt content, but with high electric potential [4].

However, the high nickel content in NMC811 leads to a high degree of cation mixing between Ni^{2+} and Li^+, resulting in capacity fade and phase change [5]. In addition, exposure of NMC811 to air forms impurities in the form of Li_2CO_3 and LiOH on its surface, causing defluorination of the binder, gas release, reacting with the electrolyte, and irreversible phase transition, thus lowering the electrochemical performance [6]-[9]. Since the electrochemical performance of NMC811 depends on crystallinity, phase purity, particle size, and structure [10]-[11]. The synthesis process of NMC811 needs to be optimized.

NMC811 can be synthesized through several methods, such as spray drying [12], sol-gel [13], hydrothermal [14], solid state [15], solution combustion [16], and coprecipitation [17]. Among the methods, coprecipitation has many advantages, such as low temperature, precise stoichiometric proportions, homogenous mixing, and ease of scalability and morphology control, thus making it the most widely used synthesis method [18]-[19]. The coprecipitation method can be classified into hydroxide coprecipitation,

DOI: 10.55981/metalurgi.2024.759

Metalurgi is Sinta 2 Journal (https://sinta.kemdikbud.go.id/journals/profile/3708) accredited by Ministry of Education, Culture, Research, and Technology, Republic Indonesia

carbonate coprecipitation, and oxalate coprecipitation [20]. Oxalate coprecipitation is cheaper and environmentally friendlier than hydroxide coprecipitation because it uses oxalic acid as a precipitating and complexing agent and does not require an inert atmosphere [21]. The precipitate is mixed with a lithium source, followed by heat treatment to obtain the final NMC [22].

Oxalate coprecipitation has been used to synthesize NMC [22]-[24]. NMC811 was synthesized by Wu et al. [21] using metal chloride salts precipitated by oxalic acid, followed by lithiation using a 1% excess lithium source. The NMC811 showed $I_{(003)}/I_{(104)}$ of 1.46 with a 200-300 nm particle size. The material provided a capacity and charge transfer resistance of 180 mAh/g and 68 Ω, respectively. Wijareni et al., [25] used sulfate metal salts to synthesize NMC811 via oxalate coprecipitation. Their results showed a circular particle with an average size of 17.16 µm with initial capacity, initial efficiency, conductivity, and lithium-ion diffusion of 178.93 mAh/g, 94.32%, 1.20×10^{-7}, and 4.22×10^{-9}, respectively. In their work, Gustiana et al., [26] used oxalate coprecipitation and compared it with hydroxide coprecipitation. Both methods resulted in spherical asymmetrical particles with a size <1 micron. They obtained that the NMC811 synthesized using oxalate coprecipitation provided higher capacity (102.42 mAh/g) than hydroxide coprecipitation (79.90 mAh/g).

In this work, NMC811 was synthesized through the oxalate coprecipitation method using metal nitrate precursors. The effects of synthesis parameters such as stirring speed, aging time, lithium amount, sintering temperature, and atmosphere were examined. To the best of the authors' knowledge, no article has reported on these synthesis parameters using the oxalate coprecipitation method. The results are given and discussed in detail in the following session.

2. MATERIALS AND METHODS

2.1 Optimization of NMC811 Synthesis

The chemicals were lithium hydroxide monohydrate ($LiOH.H_2O$), nickel (II) nitrate hexahydrate (Ni $(NO_3)_2.6H_2O$), manganese (II) nitrate tetrahydrate (Mn $(NO_3)_2.4H_2O$, cobalt (II) nitrate hexahydrate ($Co(NO_3)_2.6H_2O$, and oxalic acid ($H_2C_2O_4$), all were purchased from Sigma-Aldrich and used without any further treatment and or purification. A stoichiometric amount (8:1:1) of $Ni(NO_3)_2.6H_2O$, $Mn(NO_3)_2.4H_2O$, and $Co(NO_3)_2.6H_2O$ were dissolved into distilled water. An equimolar $H_2C_2O_4$ was also dissolved in a separate beaker in distilled water. The metal salt mixture was stirred at 60°C at three different stirring speeds (500, 750, 1000 rpm) while titrated with oxalic acid solution. The mixture was then stirred for another 2 h, without aging (aging 0 h). The mixture was then filtered, and the NMC-oxalate precipitate was dried. The three samples were labeled S-500, S-750, and S-1000, corresponding to their stirring speed. The best stirring speed was then used to determine the aging time of 0, 3, and 5 h, and the samples were labeled as A-0, A-3, and A-5, respectively. The process is illustrated in Fig. 1(a).

The best NMC-oxalate precursor sample with optimum stirring speed and aging time was then chosen to be further lithiated with $LiOH.H_2O$ through the wet milling method (300 rpm for 1 h) followed by sintering for 12 h, illustrated in Fig. 1(b). Two sintering atmospheres at 750 °C (with and without oxygen flow) with a fixed amount of lithium (5% excess) were applied, and the samples were labeled as LNMC-oxy and LNMC-air, respectively. The best sintering atmosphere was then used for the temperature variation of 700, 750, and 800 °C, labeled as LNMC-700, LNMC-750, and LNMC-800. The best sintering atmosphere and temperature were then applied for variations of lithium amount of 0, 2, and 5% excess and labeled LNMC-0, LNMC-2, and LNMC-5. The best LNMC sample, labeled as LNMC811, was then tested for electrochemical performance.

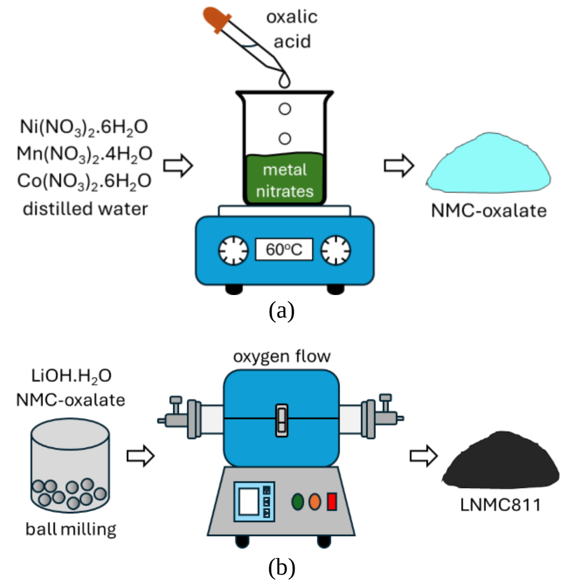

Figure 1. (a) Schematic of NMC-oxalate precursor synthesis process, and (b) lithiation of NMC-oxalate with lithium source

2.2 Characterization

Samples were characterized using Infrared spectroscopy (FTIR, Perkin Elmer) to ensure no oxalate compound remains. X-ray diffraction

(XRD, PANalytical X'Pert PRO, K-α Cu of 1.54 A) in the 2θ range of 10°–90° was used to analyze the crystal structure and the phase formed. Thermogravimetry analysis (TGA, LabSys Evo) examined thermal behaviour. In contrast, a field emission scanning electron microscope with energy dispersive X-ray spectroscopy (FESEM/EDS, FEI Inspect F-50) was used for surface morphology and elemental analysis. The electrochemical performance was carried out using electrochemical impedance spectroscopy in the frequency range of 0.1–50 kHz at 100 mV (EIS, Metrohm Autolab PGSTAT 302 N) and charge-discharge (CD, Wonatech, CCJ8F2-8 PS) to examine the conductivity and capacity, respectively.

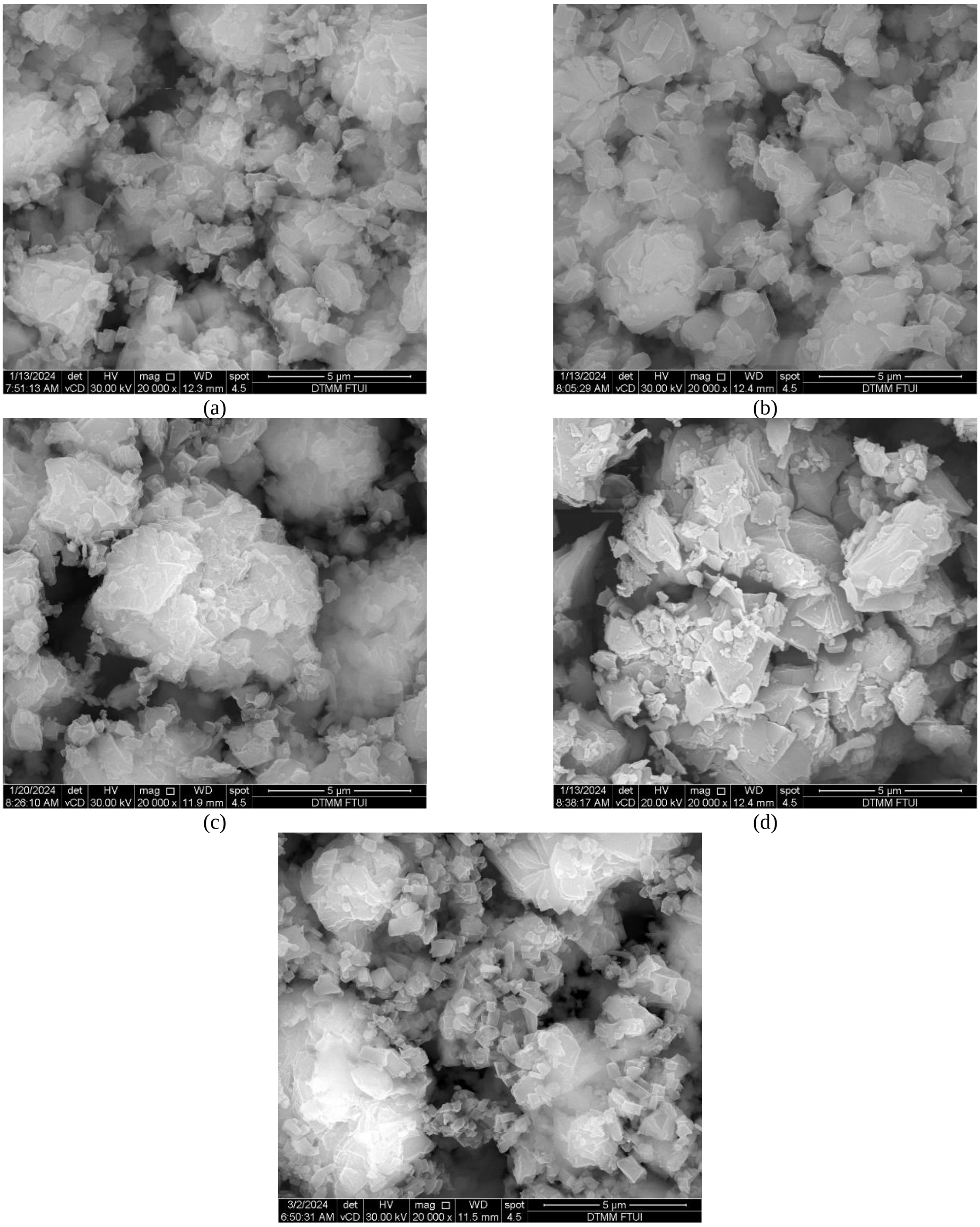

(a) (b) (c) (d) (e)

Figure 2. Electron images of (a) S-500, (b) S-750, (c) S-1000, (d) A-3, and (e) A-5

3. RESULTS AND DISCUSSION

3.1 Characteristics of NMC-oxalate

The resulting NMC-oxalate powder synthesized with different stirring speeds was characterized using FESEM (field emission scanning electron microscopy), and the results are shown in Figs. 2(a)-2(c). In contrast, the particle size analysis is listed in Table 1. The electron images show that the particles are irregularly shaped primary particles. Increasing the stirring speed from 500 to 750 rpm reduces the particle size from 0.96 to 0.77 µm. However, when the speed is increased to 1000 rpm, the particles are agglomerated with a size of 2.51 µm. This agglomeration is due to the accelerated collision among the particles [20]. Based on the FESEM results, the sample S-750 (stirring at 750 rpm with 0h aging time) has the smallest particle size and was chosen for the next variation in aging time. The reason is that the contact area between the electrode and electrolyte is increased, and the distance of Li^+ diffusion is reduced with a smaller particle size, thus increasing the electrochemical performance [26]-[27]. The morphologies of A-3 and A-5 (3 and 5h aging time, respectively) are shown in Figs. 2(d)-2(e). Analysis of the particle size (Table 1) determines that the aging time of 3 h (sample A-3) has the smallest size of 0.71, compared to A-5 and S-750 (1.02 and 0.77, respectively). Therefore, the best aging time obtained is 3 h.

Table 1. Average particle size of S-500, S-750, S-1000, A-3, A-5

Sample	Average particle size (µm)
S-500	0.96
S-750	0.77
S-1000	2.51
A-3	0.71
A-5	1.02

Characterization using infrared was conducted, and the spectra are shown in Fig. 3 (a). All samples show absorption at 3400 and 1615 cm^{-1} wavenumber, corresponding to O-H stretching and bending vibrations, respectively [28]. The 1315 and 1310 cm^{-1} peaks indicate the C-O groups [26]. Absorption around 823, 750, and 745 cm^{-1} is due to C-O and O-C=O bonds [29]. Metal oxalate is detected at wavenumber 485 cm^{-1} [30]. These results reveal information that the complexion of metal oxalate has been successfully carried out.

Sample A-3 with optimum conditions (750 rpm and 3h aging time) was further thermally analyzed before and after mixing with $LiOH.H_2O$, and the result is shown in Fig. 3(b). For sample A-3, heating to a temperature of 280°C before lithiation results in a weight loss of 20%. This corresponds to the release of two water molecules from the NMC precursor, confirming that the coprecipitation between metal nitrates and oxalic acid results in metal oxalate dihydrate following the path in Eq. 1 [23].

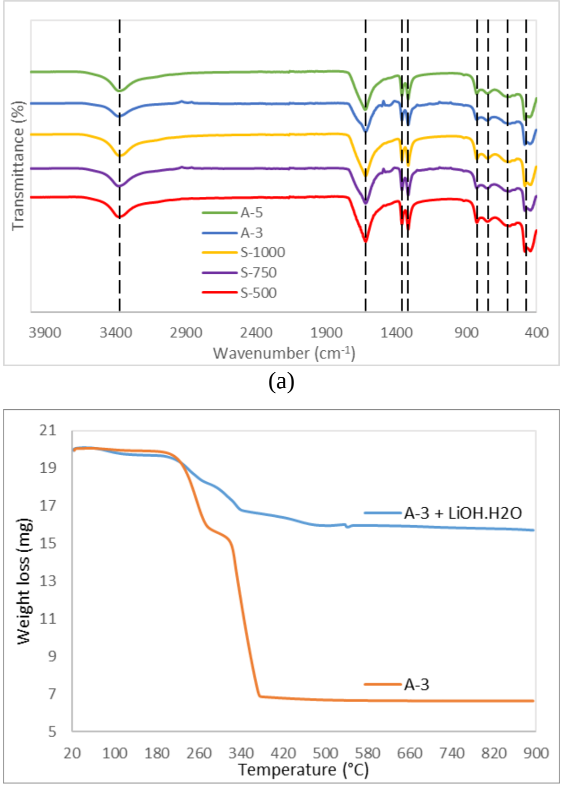

(a)

(b)

Figure 3. (a) Infrared spectra of S-500, S-750, S-1000, A-3, A-5, and (b) thermal analysis of A-3 sample before and after lithiation with $LiOH.H_2O$

The following weight loss of 57% at 380 °C from sample A-3 before lithiation is attributed to removing gaseous species from the precursor [31]. After 400 °C, no significant weight loss was detected. After lithiation, sample A-3 shows weight loss of 1.57, 7.14, 8.51, and 4.50% from room temperature to 180, 180-270, 270-350, and 350-490 °C, respectively. The loss of adsorbed water from NMC-oxalate and $LiOH.H_2O$ is for the first and second weight loss, the third is the reaction between NMC-oxalate and oxygen, and the last one is the formation of the final NMC following the path given in Eqs. 2-5 [32]-[34]. Similar results were also observed in another study [27].

$$0.8Ni(NO_3)_2.6H_2O_{(aq)} + 0.1Mn(NO_3)_2.4H_2O_{(aq)} + 0.1Co(NO_3)_2.6H_2O_{(aq)} + H_2C_2O_{4(aq)} \rightarrow Ni_{0.8}Mn_{0.1}Co_{0.1}C_2O_4.2H_2O_{(s)} + 2HNO_{3(aq)} + 3.8H_2O_{(aq)} \quad (1)$$

$$Ni_{0.8}Mn_{0.1}Co_{0.1}C_2O_4.2H_2O_{(s)} \rightarrow Ni_{0.8}Mn_{0.1}Co_{0.1}C_2O_{4(s)} + 2H_2O_{(g)} \quad (2)$$

$$2LiOH.H_2O_{(s)} \rightarrow Li_2O_{(s)} + 3H_2O_{(g)} \quad (3)$$

$$Ni_{0.8}Mn_{0.1}Co_{0.1}C_2O_{4\,(s)} + O_{2\,(g)} \rightarrow Ni_{0.8}Mn_{0.1}Co_{0.1}O_{2\,(s)} + 2CO_{2\,(g)} \quad (4)$$

$$2Ni_{0.8}Mn_{0.1}Co_{0.1}O_{2\,(s)} + Li_2O_{(s)} \rightarrow 2LiNi_{0.8}Mn_{0.1}Co_{0.1}O_{2\,(s)} + 0.5O_{2\,(g)} \quad (5)$$

3.2 Characteristics of NMC811

In the thermal analysis, the lithiated NMC-oxalate was sintered in two conditions, with and without oxygen flow. In Figure 4 (a), LNMC-air and LNMC-oxy show similar spectra with small absorption at 880 and 1400 cm^{-1}. These can be attributed to incomplete burning of oxalate or the formation of Li_2CO_3 impurities due to excess lithium [29].

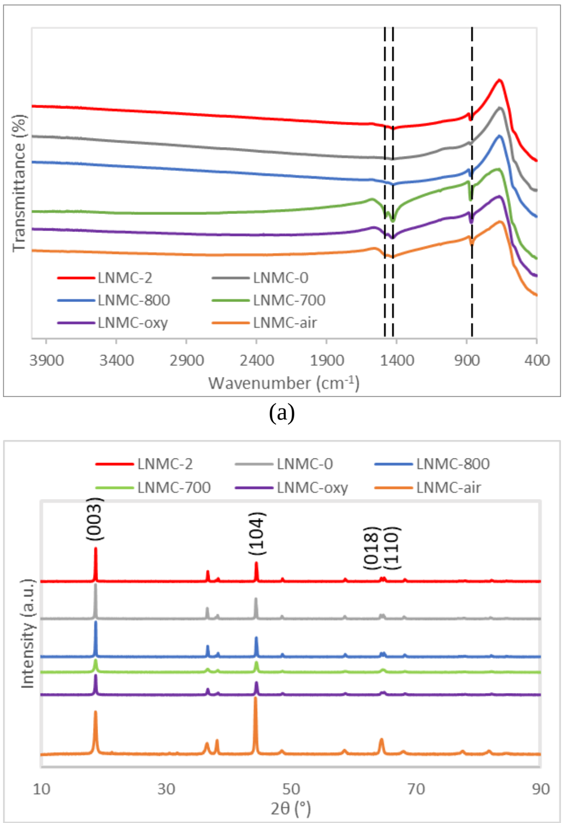

(a)

(b)

Figure 4. (a) Infrared spectra and (b) X-ray diffractograms of LNMC samples

Further characterization using XRD was conducted to confirm this proposition. Analysis of the X-ray diffractograms of all LNMC samples except LNMC-air (shown in Fig. 4(b)) match with reference ICDD 01-070-4314 (lithium nickel manganese cobalt oxide with layered rhombohedral structure and R-3m space group) with no impurities detected. However, LNMC-air matches with lithium nickel oxide (reference 01-077-2126), showing that manganese and cobalt were not incorporated into the structure. These results show that oxygen is important in the sintering process of NMC811, primarily because of the lower bonding energy between Ni^{3+} and O^{2-}, resulting in oxygen loss from the nickel-rich material structure during the sintering process [35]-[36].

LNMC-air and LNMC-oxy samples analyzed using FESEM (Figs. 5(a)-5(b)) show semicircular-shaped particles with an average particle size of 61 nm and 69 nm (Table 2), respectively.

Based on the characterization results, the sintering condition with oxygen flow was then used to determine the sintering temperature. Infrared spectra shown in Fig. 4(a), purple, green, and blue lines correspond to the sintering temperatures of 700, 750, and 800°C, respectively. The sample sintered at 700°C shows a sharper absorption around 880 and 1400 cm^{-1}. There is a possibility that, because of the low sintering temperature, the removal of oxalate from the structure is incomplete. This can also be observed from the FESEM image in Fig. 5(c), which shows irregular particles (51 nm) compared to the particles sintered at 750 and 800°C that are semicircular (69 and 58 nm) (Figs. 5(b)-5(d)). Further, the XRD results in Fig. 4(b) confirm that LNMC-700 shows no clear peak splitting (018)/(110) and has a low-intensity ratio of peak (003)/(104), which is only 1.16. The clear peak (018)/(110) splitting and I(003)/I(104) ratio higher than 1.20 are indications of a well-ordered layered structure and low cation mixing [37]-[38]. Sintering at 800°C resulted in a high I(003)/I(104) of 1.67, higher than 750°C (1.47). It can then be concluded that the optimum sintering temperature is 800°C.

The effect of lithium concentration is investigated by conducting the sintering process under an oxygen atmosphere at 800°C, with a variation of 0, 2, and 5% excess lithium. The electron images in Figs. 5(d)-5(f) show that all samples possess semicircular particles with the smallest particle size of 57 nm for the LNMC-2 sample. Infrared results of these samples show little absorption around 880 and 1400 cm^{-1} compared to other LNMC samples, meaning that the removal of oxalate is completed and no impurities of lithium compounds. This is confirmed by XRD characterization. The highest $I_{(003)}/I_{(104)}$ ratio is exhibited by sample LNMC-2 (Table 2), which is 1.70.

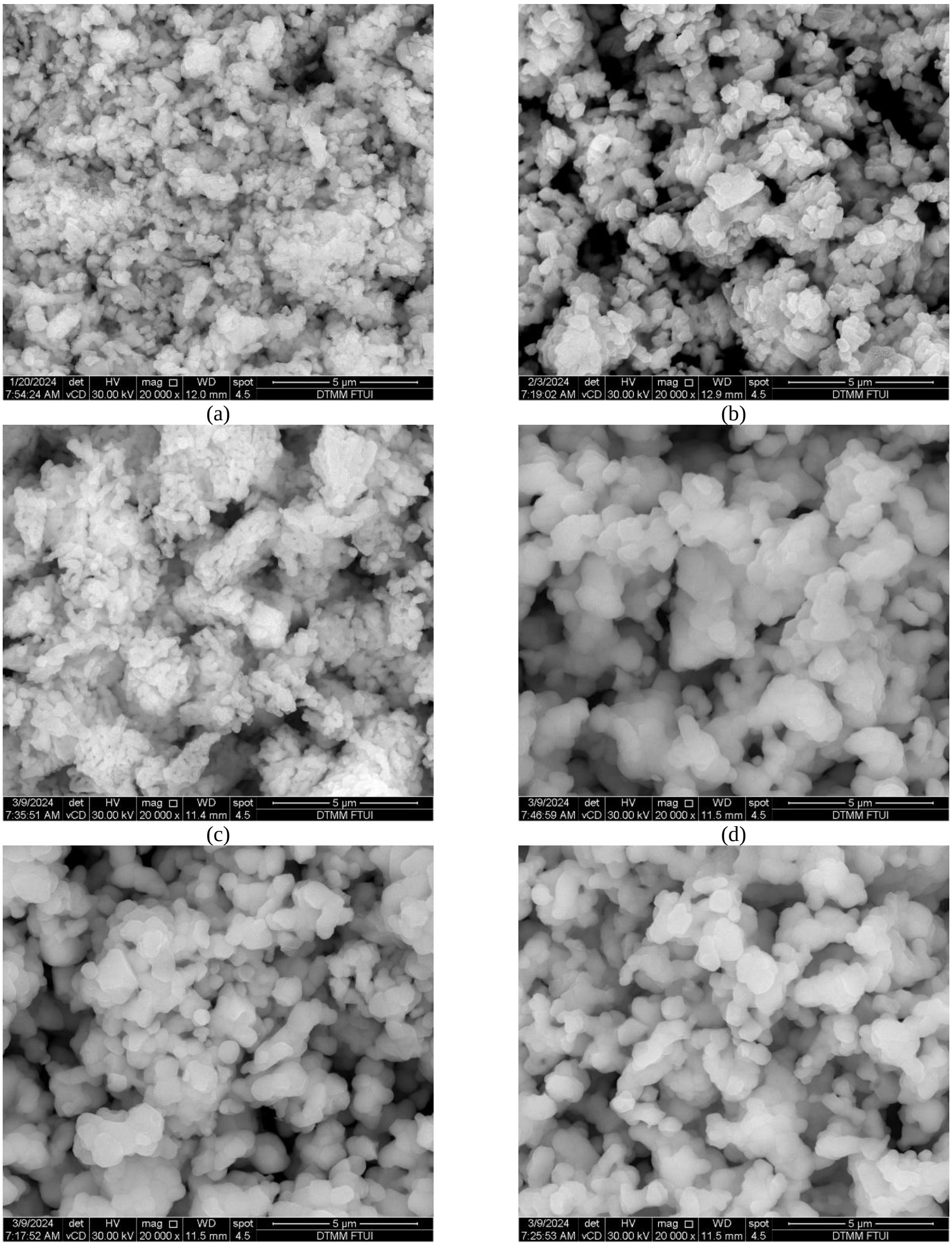

(a) (b)

(c) (d)

(e) (f)

Figure 5. Electron images of (a) LNMC-air, (b) LNMC-oxy, (c) LNMC-700, (d) LNMC-800, (e) LNMC-0, and (f) LNMC-2

In conclusion, the optimum parameters are using 2% excess lithium, sintering temperature at 800°C under oxygen flow. This sample is then labeled as LNMC811 and characterized using EDS. The detected elements listed in Table 3 show that the nickel, manganese, and cobalt ratio confirms the amount used in the synthesis.

Figure 6(a) shows the EIS result of the LNMC811 sample. Equation 1 is used to calculate the conductivity (Ω), where l is the thickness (150 µm) and A is the area (2.14 cm^2) of the sample. The charge transfer resistance (R_{ct}) measured for the LNMC811 sample is 261.4 Ω, resulting in a 2.68 x 10^{-5} S/cm conductivity. This result is similar to the result from another study [16]. The charge-discharge graph in Fig. 6(b) shows the initial charge and discharge capacity of LNMC811 (229.73 and 212.93 mAh/g, respectively) with a coulombic efficiency of 92.68%. The discharge capacity of this work is higher compared to other studies conducted by Wu et al. (discharge capacity of 178 mAh/g) [21], Wijareni et al. (178.93 mAh/g) [25], and Gustiana et al. (102.42 mAh/g) [26]. Figure 6(a) shows the EIS result of the LNMC811 sample.

Equation 1 is used to calculate the conductivity (Ω), where l is the thickness (150 µm) and A is the area (2.14 cm^2) of the sample.

Table 2. Average particle size and I(003)/I(104) of LNMC samples

Sample	Lithium amount	Sintering temperature (°C)	Average particle size (nm)	$I_{(003)}/I_{(10}$
LNMC-air	5% excess	750	61	0.78
LNMC-oxy (LNMC-750)			69	1.47
LNMC-700		700	51	1.16
LNMC-800 (LNMC-5)		800	58	1.67
LNMC-0	0% excess		60	1.61
LNMC-2	2% excess		57	1.70

The charge transfer resistance (R_{ct}) measured for the LNMC811 sample is 261.4 Ω, resulting in a 2.68 x 10^{-5} S/cm conductivity.

Table 3. Elemental composition of LNMC811

Element (wt.%)	Ni	Mn	Co	O
LNMC811	57.95	4.98	8.96	28.11

This result is similar to the result from another study [16].

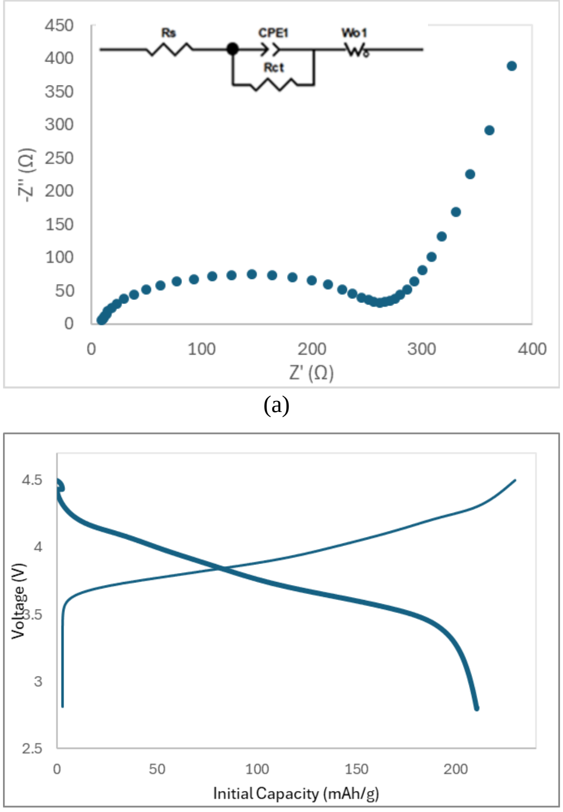

(a)

(b)

Figure 6. (a) Nyquist plot, (b) initial charge-discharge capacity of LNMC811

The charge-discharge graph in Fig. 6(b) shows the initial charge and discharge capacity of LNMC811 (229.73 and 212.93 mAh/g, respectively) with a coulombic efficiency of 92.68%. The discharge capacity of this work is higher compared to other studies conducted by Wu et al. (discharge capacity of 178 mAh/g) [21], Wijareni et al. (178.93 mAh/g) [25], and Gustiana et al. (102.42 mAh/g) [26].

4. CONCLUSION

This study examined the synthesis parameters such as stirring speed, aging time, lithium amount, sintering atmosphere, and temperature to determine the optimum parameters for NMC811 synthesis. Increasing stirring speed (750 rpm) and aging time (3 hours) in the synthesis of NMC811 oxalate precursor resulted in a smaller particle size of 0.71 µm. Lithium amount (2% excess) and sintering conditions (800 °C under oxygen flow) are important to obtain the crystalline structure with low cation mixing and impurities. These optimum conditions result in high electrochemical performance of NMC811 with a coulombic efficiency of 92.68% and a 212.93 mAh/g capacity. These results are promising for the synthesis of NMC811 with a simple and cheap process that does not require an inert atmosphere.

ACKNOWLEDGMENT

This research is funded by the Indonesian Endowment Fund for Education (LPDP) on behalf of the Indonesian Ministry of Education, Culture, Research, and Technology, and managed under the INSPIRASI Program (Contract No. 6635/E3/KL.02.02/2023)

REFERENCES

[1] R. Sharma, H. Kumar, G. Kumar, S. Sharma, R. Aneja, A. K. Sharma, R. Kumar, and P. Kumar, “Progress and challenges in electrochemical energy storage devices: Fabrication, electrode material, and economic aspects,” *Chemical Engineering Journal*, vol. 468, p. 143706, 2023. DOI: 10.1016/j.cej.2023.143706.

[2] J. Yang, X. Liang, H. Ryu, C. S. Yoon, and Y. Sun, “Ni-rich layered cathodes for lithium-ion batteries : From challenges to the future,” *Energy Storage Mater*, vol. 63, p. 102969, 2023. DOI: 10.1016/j.ensm.2023.102969.

[3] B. Xiao and X. Sun, “Surface and subsurface reactions of Lithium transition metal oxide cathode materials: An overview of the fundamental origins and remedying approaches,” *Adv Energy*

Mater, vol. 8, no. 29, pp. 1-27, 2018. DOI: 10.1002/aenm.201802057.

[4] J. V. Laveda, J. E. Low, F. Pagani, E. Stilp, S. Dilger, V. Baran, M. Heere, and C. Battaglia, “Stabilizing capacity retention in NMC811/graphite full cells via TMSPi Electrolyte Additives,” *ACS Appl Energy Mater*, vol. 2, no. 10, pp. 7036-7044, 2019. DOI: 10.1021/acsaem.9b00727.

[5] P. Yan, J. Zheng, L. Dongping, Y. Wei, J. Zheng, Z. Wang, S. Kuppan, J. Yu, L. Luo, D. Edwards, M. Olszta, K. Amine, J. Liu, J. Xiao, F. Pan, G. Chen, J. G. Zhang, and C. M. Wang, “Atomic-resolution visualization of distinctive chemical mixing behavior of Ni, Co, and Mn with Li in layered Lithium transition-metal oxide cathode materials,” *Chemistry of Materials*, vol. 27, no. 15, pp. 5393-5401, 2015. DOI: 10.1021/acs.chemmater.5b02016.

[6] S. T. Myung, F. Maglia, K. J. Park, C. S. Yoon, P. Lamp, S. J. Kim, and Y. K. Sun, “Nickel-rich layered cathode materials for automotive Lithium-ion batteries: Achievements and perspectives,” *ACS Energy Letters*, vol. 2, no. 1, pp. 196-223, 2017. DOI: 10.1021/acsenergylett.6b00594.

[7] S. E. Renfrew and B. D. McCloskey, “Residual Lithium carbonate predominantly accounts for first cycle CO_2 and CO outgassing of Li-stoichiometric and Li-rich layered transition-metal oxides,” *J Am Chem Soc*, vol. 139, no. 49, pp. 17853-17860, 2017. DOI: 10.1021/jacs.7b08461.

[8] Y. Bi, T. Wang, M. Liu, R. Du, W. Yang, Z. Liu, Z. Peng, Y. Liu, D. Wang, and X. Sun, “Stability of Li_2CO_3 in cathode of lithium ion battery and its influence on electrochemical performance,” *RSC Adv*, vol. 6, no. 23, pp. 19233-19237, 2016. DOI: 10.1039/c6ra00648e.

[9] A. Manthiram, J. C. Knight, S. T. Myung, S. M. Oh, and Y. K. Sun, “Nickel-rich and Lithium-rich layered oxide cathodes: Progress and perspectives,” *Adv Energy Mater*, vol. 6, no. 1, 2016. DOI: 10.1002/aenm.201501010.

[10] H. Zhang, H. Zhao, M. A. Khan, W. Zou, J. Xu, L. Zhang, and J. Zhang, “Recent progress in advanced electrode materials, separators and electrolytes for lithium batteries,” *J Mater Chem A Mater*, vol. 6, p. 20564, 2018. DOI: 10.1039/c8ta05336g.

[11] L. J. Li, X. H. Li, Z. X. Wang, H. J. Guo, P. Yue, W. Chen, and L. Wu, “A simple and effective method to synthesize layered $LiNi_{0.8}Co_{0.1}Mn_{0.1}O_2$ cathode materials for lithium ion battery,” *Powder Technol*, vol. 206, pp. 353-357, 2011. DOI: 10.1016/j.powtec.2010.09.010.

[12] B. Lin, Z. Wen, Z. Gu, and S. Huang, “Morphology and electrochemical performance of $Li[Ni1/3Co1/3Mn1/3O_2]$ cathode material by a slurry spray drying method,” *J Power Sources*, vol. 175, no. 1, pp. 564-569, 2008. DOI: 10.1016/j.jpowsour.2007.09.055.

[13] J. Xu, S. L. Chou, Q. F. Gu, H. K. Liu, and S. X. Dou, “The effect of different binders on electrochemical properties of LiNi $1/3Mn1/3Co1/3O_2$ cathode material in Lithium ion batteries,” *J Power Sources*, vol. 225, pp. 172-178, 2013. DOI: 10.1016/j.jpowsour.2012.10.033.

[14] Q. Jing, J. Zhang, C. Yang, Y. Chen, and C. Wang, “A novel and practical hydrothermal method for synthesizing $LiNi1/3Co1/3Mn1/3O_2$ cathode material,” *Ceram Int*, vol. 46, no. 12, pp. 20020-20026, 2020. DOI: 10.1016/j.ceramint.2020.05.073.

[15] L. Tang, X. Cheng, R. Wu, T. Cao, J. Lu, Y. Zhang, and Z. Zhang, “Monitoring the morphology evolution of $LiNi0.8Mn0.1Co0.1O_2$ during high-temperature solid state synthesis via in situ SEM,” *Journal of Energy Chemistry*, vol. 66, pp. 9-15, 2022. DOI: 10.1016/j.jechem.2021.07.021.

[16] F. Angellinnov, A. Subhan, A. J. Drew, and A. Z. Syahrial, “Synthesis of Sn doped and rice husk derived activated carbon surface coating NMC 811 through solution combustion method,” *Heliyon*, vol. 10, no. 1, p. e23199, 2024. DOI: 10.1016/j.heliyon.2023.e23199.

[17] A. L. Lipson, B. J. Ross, J. L. Durham, D. Liu, M. Leresche, T. T. Fister, L. Liu, and K. Kim, “Stabilizing NMC 811 Li-ion battery cathode through a rapid coprecipitation process,” *Applied Energy Materials*, vol. 4, pp. 1972-1977, 2021. DOI: 10.1021/acsaem.0c03112.

[18] X. Zhao, J. Wang, X. Dong, G. Liu, W. Yu, and L. Wang, “Structure design and performance of $LiNixCoyMn1\text{-}x\text{-}yO_2$ cathode materials for lithium-ion batteries: A review,” *Journal of the*

Chinese Chemical Society, vol. 61, no. 10, pp. 1071-1083, 2014. DOI: 10.1002/jccs.201400107.

[19] H. Li, Q. Xu, X. X. Shi, D. W. Song, and L. Q. Zhang, "Electrochemical performance of LiNi0.5Mn0.5O$_2$ with different synthesis methods," *Rare Metals*, vol. 34, no. 8, pp. 580-585, 2015. DOI: 10.1007/s12598-013-0088-z.

[20] M. Malik, K. H. Chan, and G. Azimi, "Review on the synthesis of LiNixMnyCo1-x-yO$_2$ (NMC) cathodes for lithium-ion batteries," *Mater Today Energy*, vol. 28, p. 101066, 2022. DOI: 10.1016/j.mtener.2022.101066.

[21] C. Y. Wu, Q. Bao, Y. T. Tsai, and J. G. Duh, "Tuning (003) interplanar space by boric acid co-sintering to enhance Li+ storage and transfer in Li(Ni0.8Co0.1Mn0.1)O$_2$ cathode," *J Alloys Compd*, vol. 865, p. 158806, 2021. DOI: 10.1016/j.jallcom.2021.158806.

[22] H. Tian, N. Ye, D. Liu, and W. Li, "Effects of synthesis conditions on the structural and electrochemical properties of layered LiNi1/3Co1/3Mn1/3O$_2$ cathode material via oxalate co-precipitation method," *Rare Metals*, vol. 27, no. 6, pp. 575-579, 2008. DOI: 10.1016/S1001-0521(08)60185-0.

[23] C. F. Zhang, P. Yang, X. Dai, X. Xiong, J. Zhan, and Y. L. Zhang, "Synthesis of LiNi1/3Co1/3Mn1/3O$_2$ cathode material via oxalate precursor," *Transactions of Nonferrous Metals Society of China (English Edition)*, vol. 19, no. 3, pp. 635-641, 2009. DOI: 10.1016/S1003-6326(08)60325-8.

[24] A. Jihad, A. A. N. Pratama, C. S. Yudha, M. Rahmawati, H. Widiyandari, and A. Purwanto, "Effect of Zn, Cu, and Mg doping on the structural characteristic of LiNi0.6Mn0.2Co0.2O$_2$ (NMC622)," in *ACM International Conference Proceeding Series Association for Computing Machinery*, 2020. DOI: 10.1145/3429789.3429857.

[25] A. S. Wijareni, H. Widiyandari, A. Purwanto, A. F. Arif, and M. Z. Mubarok, "Morphology and particle size of a synthesized NMC 811 cathode precursor with mixed hydroxide precipitate and Nickel sulfate as Nickel sources and comparison of their electrochemical performances in an NMC 811 Lithium-ion battery," *Energies (Basel)*, vol. 15, no. 16, p. 5794, 2022. Doi: 10.3390/en15165794.

[26] H. S. E. A. Gustiana, F. R. Agustiana, S. S. Nisa, and E. R. Dyartanti, "Synthesis and characterization of NMC 811 by oxalate and hydroxide coprecipitation method," *Evergreen*, vol. 9, no. 2, pp. 438–442, 2022. Doi: 10.5109/4794169.

[27] D. Wang, I. Belharouak, G. Zhou, and K. Amine, "Synthesis of Lithium and Manganese-rich cathode materials via an oxalate co-precipitation method," *J Electrochem Soc*, vol. 160, no. 5, pp. A3108-A3112, 2013. Doi: 10.1149/2.016305jes.

[28] H. Widiyandari, R. Ardiansah, and A. S. Wijareni, "Synthesis of lithium nickel manganese cobalt as cathode material for Li-ion battery using different precipitant agents by coprecipitation method," *AIP Conf Proc of the 2020 International Conference on Engineering and Information Technology for Sustainable Industry*, vol. 2217, pp. 030023-1-030023-8, 2020. DOI:10.1145/3429789.3429857.

[29] S. S. Nisa, M. Rahmawati, C. S. Yudha, H. Nilasary, H. Nursukatmo, H. S. Oktaviano, S. U. Muzayanha, and A. Purwanto, "Fast approach to obtain layered transition-metal cathode material for rechargeable batteries," *Batteries*, vol. 8, no. 1, 2022. DOI: 10.3390/batteries8010004.

[30] I. Jung, J. Choi, and Y. Tak, "Nickel oxalate nanostructures for supercapacitors," *J Mater Chem*, vol. 20, no. 29, pp. 6164-6169, 2010. DOI: 10.1039/c0jm00279h.

[31] A. Habibi, M. Jalaly, R. Rahmanifard, and M. Ghorbanzadeh, "Solution combustion synthesis of the nanocrystalline NCM oxide for lithium-ion battery uses," *Mater Res Express*, vol. 5, no. 2, 2018. DOI: 10.1088/2053-1591/aaab12.

[32] M. Satyanarayana, A. K. Jibin, E. Umeshbabu, J. James, and U. V. Varadaraju, "Optimizing conditions and improved electrochemical performance of layered LiNi1/3Co1/3Mn1/3O$_2$ cathode material for Li-ion batteries," *Ionics (Kiel)*, vol. 28, no. 1, pp. 229-240, 2022. DOI: 10.1007/s11581-021-04297-2.

[33] R. Zhao, Z. Yang, J. Liang, D. Lu, C. Liang, X. Guan, A. Gao, and H. Chen,

"Understanding the role of Na-doping on Ni-rich layered oxide LiNi0.5Co0.2Mn0.3O2," *J Alloys Compd*, vol. 689, pp. 318-325, 2016. DOI: 10.1016/j.jallcom.2016.07.230.

[34] Z. Qiu, Y. Zhang, P. Dong, S. Xia, and Y. Yao, "A facile method for synthesis of LiNi0.8Co0.15Al0.05O_2 cathode material," *Solid State Ion*, vol. 307, pp. 73-78, 2017. DOI: 10.1016/j.ssi.2017.04.011.

[35] K. Meng, Z. Wang, H. Guo, and X. Li, "Enhanced cycling stability of LiNi0.8Co0.1Mn0.1O_2 by reducing surface oxygen defects," *Electrochim Acta*, vol. 234, pp. 99-107, 2017. DOI: 10.1016/j.electacta.2017.03.054.

[36] H. J. Noh, S. Youn, C. S. Yoon, and Y. K. Sun, "Comparison of the structural and electrochemical properties of layered Li[NixCoyMnz]O_2 (x = 1/3, 0.5, 0.6, 0.7, 0.8 and 0.85) cathode material for lithium-ion batteries," *J Power Sources*, vol. 233, pp. 121-130, 2013. DOI: 10.1016/j.jpowsour.2013.01.063.

[37] M. Zhang, J. Shen, J. Li, D. Zhang, Y. Yan, Y. Huang, and Z. Li, "Effect of micron-sized particle on the electrochemical properties of nickel-rich LiNi0.8Co0.1Mn0.1O_2 cathode materials," *Ceram Int*, vol. 46, no. 4, pp. 4643-4651, 2020. DOI: 10.1016/j.ceramint.2019.10.195.

[38] H. Gu, J. Wang, Z. Wang, J. Tong, N. Qi, G. Han, and M. Zhang, "Self-assembled porous LiNi0.8Co0.1Mn0.1O_2 cathode materials with micro/ nano-layered hollow morphologies for high-power lithium-ion batteries," *Appl Surf Sci*, vol. 539, p. 148034, 2021. DOI: 10.1016/j.apsusc.2020.148034.

Metalurgi (2024) 2: 89 - 96

BRIN
BADAN RISET
DAN INOVASI NASIONAL

METALURGI
Majalah Ilmu dan Teknologi
p-ISSN 0126-3188 | e-ISSN 2443-3926
ejurnalmaterialmetalurgi.lipi.go.id

STUDY ON LEACHING LANTHANUM FROM FERRONICKEL SLAG WITH PRETREATMENT ALKALINE FUSION

Fakhruddin Yudomustafa[1], Eni Febriana[2], Wahyu Mayangsari[2], Nurhayati Indah Ciptasari[2*], Ari Yustisia Akbar[2], Hendrik[2], Soesaptri Oediyani[1], Agus Budi Prasetyo[2]
[1]Department of Metallurgy, Sultan Ageng Tirtayasa University
Jl. Jenderal Sudirman Km 3, Cilegon, Banten, Indonesia 42435
[2]Research Center for Metallurgy, National Research and Innovation Agency (BRIN)
B.J. Habibie Sains and Technology Area, Banten, Indonesia 15314
*Email: nurh024@brin.go.id

Received: 15-1-2024, Revised: 11-04-2024, Accepted: 11-04-2025

Abstract

Ferronickel slag is a byproduct of nickel ore smelting. Several efforts have been made to find alternative applications for ferronickel slag, such as the production of construction materials, cement, or geopolymers. It is reported that 38% is used for road construction, 48% is used for industrial cement mixtures, and the rest is used for fertilizers, geopolymers, and hydraulic techniques. Ferronickel slag still contains some valuable minerals such as silica, magnesium, nickel, iron, and several REEs (rare earth elements). One of the REEs, namely lanthanum, has many applications, including Ni-MH (nickel-metal hydride) batteries, phosphors for lamps, fluid-cracking catalysts for oil refining, LaNi5 for hydrogen gas storage, metal alloys for cast iron, steel and magnesium alloys, additives for glassware (for cameras), and lanthanum hexaboride ceramic. In connection with the slag, which contains impurities in strong silica compounds, it is necessary to carry out an alkaline fusion treatment. Alkaline fusion was carried out by varying the time from 0.5 to 4 hours and the ratio of the mass of slag to NaOH: 1:0.6, 1:1, 1:1.23, 1:1.47, and 1:1.84. The biggest decrease in SiO_2 *was in the 3-hour alkaline fusion time, from 48.347% to 27.3%, and in the mass ratio at 1:1.47, from 48.347% to 21.413%. This research aims to provide added value for ferronickel slag by extracting lanthanum by acid leaching using* H_2SO_4 *reagent by varying the time (5, 10, 30, 60, and 120 minutes), temperature (30, 60, and 90 °C), and concentration (1, 2, and 3 M). The results showed that the best leaching point was at 5 minutes, 30 °C, and 1 M, yielding a lanthanum extraction percentage of 38.082%.*

Keywords: *Acid leaching, added value, alkali fusion, ferronickel slag, lanthanum*

1. INTRODUCTION

Ferronickel slag is a byproduct of nickel ore smelting. Ferronickel slag is designated as hazardous and toxic waste for the environment with a danger level 2 (i.e., it has delayed effects and does not directly influence humans) by Government Regulation (PP) Number 101 of 2014. Therefore, based on the Ministerial Regulation of the Ministry of Environment and Forestry, Chapter I, Article 2, storage and disposal of B3 waste are required. Currently, Ferronickel slag is only used as a construction material and is merely piled in one place [1]. Numerous attempts are underway to find alternate uses for ferronickel slag, including the creation of cement, geopolymer, and building materials [2].

Reported that the main compound in ferronickel slag was silica in the form of SiO_2 at 45.69%. Based on XRD (x-ray diffraction) analysis [3], ferronickel slag is dominated by magnesium silicate and iron silicate, which are formed by forsterite (Mg_2SiO_4), enstatite ($MgSiO_3$), and fayalite (Fe_2SiO_4). To form an amorphous structure, the furnace's slag can be

DOI: 10.55981/metalurgi.2024.764

Metalurgi is Sinta 2 Journal (https://sinta.kemdikbud.go.id/journals/profile/3708) accredited by Ministry of Education, Culture, Research, and Technology, Republic Indonesia

cooled using air cooling or granulation techniques [4].

Ferronickel slag retains important minerals, including silica, magnesium, nickel, iron, and several REEs (rare earth elements). The main components of ferronickel slag are silica (Si) at 30%, magnesium (Mg) at 20%, iron (Fe) at 12%, and aluminum (Al) at 1-2%, along with other elements [1]. A study [3] reported that the REEs contained ferro-nickel slag. Lanthanum, a rare earth element, is used in a variety of products, such as phosphor for lamps, fluid-cracking catalysts for oil refining, $LaNi_5$ for storing hydrogen gas, metal alloys for cast iron, steel, and magnesium, glass additives (for cameras), and lanthanum hexaboride ceramic [5].

Regarding slag containing impurities in the form of strong silica compounds [6], the separation of silica is very important in improving the recovery of valuable metals from ferronickel slag [2]. Several treatments have been conducted [7] with the caustic leaching process under NaOH concentration 5 N, temperature 80 °C, and time 4 hours, resulting in a soluble silica content of 18.4%. Alkali pugging with slag conditions: NaOH mass ratio 1:2, temperature 250 °C, and time 4 hours resulted in a soluble silica content of 35.2%. Alkali fusion with slag conditions: NaOH mass ratio 1:1, temperature 650 °C, and time 4 hours resulted in a soluble Si content of 35-37%. Another study was conducted by [8] with alkali fusion treatment on zircon tailings with a sample size of 180 mm, a temperature of 450 °C, a duration of 3 hours, and a mass ratio of 1:1, resulting in a dissolved Si content of 66%. Alkali fusion is classified as wet decomposition, which involves the addition of a base (commonly NaOH) followed by heating at a specific time and temperature [6].

In this study, alkali fusion treatment was performed on samples by varying the alkali fusion time of 0.5, 1, 2, 3, and 4 hours and the mass ratio of slag: NaOH 1:0.6; 1:1; 1:1.23; 1:1.47; and 1:1.83 to initially study the effect of temperature and duration on alkali fusion to reduce SiO_2 content. The sodium silicate created during the alkali fusion process was dissolved by water leaching, which increased lanthanum in the water-leaching residue. This is anticipated to be used as a reference for thermodynamic factors in the alkali fusion process for handling ferronickel slag.

Additionally, this research aims to add value to ferronickel slag by leaching with sulfuric acid (H_2SO_4) reagent to recover lanthanum metal. The selection of H_2SO_4 reagent in acid leaching was based on research on lanthanum leaching from a hydrocracking catalyst. The result was that lanthanum recovered 90.836% [9]. According to the study on the leaching of REEs from tin slag II, the percentage of extraction increases as the temperature rises between 30 and 90 °C [2]. The study's findings on the influence of reagent concentration showed that using H_2SO_4 reagent to leach lanthanum from red mud enhanced recovery as concentration increased between 1 and 3 M [10]. The effect of time-based leaching REEs from tin slag II was then varied to 5, 10, 30, 60, and 120 minutes; the resulting leaching occurred in rapid time [2].

2. MATERIALS AND METHODS

2.1 Materials

The raw materials used in this research are ferronickel slag collected from PT ANTAM Pomaalaa. A ball mill milled the ferronickel slag to obtain a -200 particle size mesh. Characterization of ferronickel slag used XRD to determine the phase formed in ferronickel slag. XRF is used to determine the chemical composition of ferronickel slag. ICP-OES to determine rare earth elements in ferronickel slag, especially lanthanum.

2.2 Methods

The experiment was executed in three phases: acid leaching, water leaching, and alkaline fusion. The investigation uses ICP-OES (inductively coupled plasma-optical emission spectrometry), XRD (x-ray diffraction), and XRF (x-ray fluorescence) as analytical methods [2].

2.3 Alkali Fusion

Alkali fusion mixture of ferronickel slag: NaOH by physical blending. The mixture sample was weighed and put into the crucible. The sample was performed in a muffle furnace. This research employed time variations of alkali fusion (30, 60, 120, 180, and 240 minutes) and mass ratio modifications of ferronickel slag with NaOH (1:0.6; 1:1; 1:1.23; 1:1.47; 1:1.84). The alkali fusion temperature was established at 150 °C.

2.4 Water Leaching

Product alkali fusion named frit was then water leached using distilled water with a conditioning temperature of 90 °C, leaching time of 60 minutes, and S/L 1/5 g/mL. Water leaching aims to dissolve silica as sodium silica from alkali fusion. Filtrate and residue are the end products of the water-leaching process. After water leaching, the sample was filtered to separate the filtrate and residue. The residue from the leaching of water, which will be used as raw material for leaching, is dried using an oven at 105 °C, and the filtrate from the leaching is analyzed by ICP-OES analysis to determine the level of dissolved impurities during the water leaching process.

2.5 Acid Leaching

The residue is dissolved with H_2SO_4 and placed in the reactor glass to begin the acid-leaching process. Solid/Liquid (S/L) 10/100 g/mL, 200 rpm stirring rate, concentration variations of 1, 2, and 3 M, followed by variations in leaching duration for 5, 10, 30, 60, and 120 minutes, and temperature variation for 30; 60; and 90°C, were the conditions under which acid leaching was conducted. After acid leaching, filtration was carried out to produce filtrate in the form of PLS (pregnant leaching solution) and residue. The filtrate was examined via ICP-OES, whereas the residue was assessed using XRF.

3. RESULTS AND DISCUSSION

3.1 Characterization of Ferronickel Slag

Table 1 presents the findings of the characterization of the first ferronickel slag via XRF analysis.

Table 1. The result of the characterization of ferronickel slag using XRF analysis

Compounds	Wt.%
SiO_2	48.347
Cr_2O_3	1.931
Al_2O_3	5.946
MgO	27.263
Fe_2O_3	13.427
Others	3.084

The dominant compounds in ferronickel slag are SiO_2, MgO, and Fe_2O_3, which are 48.347%, 27.263%, and 13.427%, respectively.

Table 2. The result of the characterization of ferronickel slag using ICP-OES analysis

Element	Wt (ppm)
Ce	1109
La	347
Nd	303
Pr	71
Y	112
Sm	116

This is consistent with several previous studies that state that the most dominant composition in ferronickel slag is silica oxide [11]-[14].

Table 2 presents the characterization results of the first REEs, particularly lanthanum (La), in the initial ferronickel slag, revealing a concentration of 347 ppm of lanthanum.

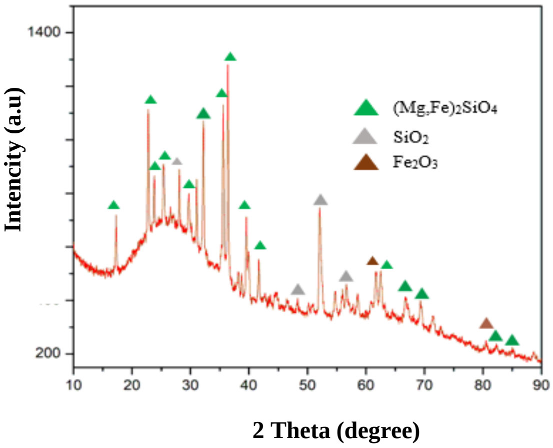

Figure 1. The result of the characterization of ferronickel slag used XRD analysis

Figure 1 illustrates the outcomes of the characterization of preliminary ferronickel slag using XRD analysis. In line with earlier research, the primary components that predominated in ferronickel slag were olivine $(Mg,Fe)_2SiO_4$, silica (SiO_2), and hematite (Fe_2O_3) at the main phase [15]-[17].

3.2 Alkali Fusion

3.2.1 Effect of Time on SiO_2 Removal

The effect of time on SiO_2 removal after alkaline fusion is shown in Fig. 2. The effect of time on the results of SiO_2 levels is that the longer the alkali fusion time, the greater the SiO_2 in ferronickel slag reacts with NaOH to form Na_2SiO_3. This phenomenon is due to the principle of the reaction rate, namely, the reactant decreases with increasing time, and the product increases as time increases time [18].

However, after 240 minutes, there was an increase from 27.3% to 27.4%. This is possible because after 3 hours, the reaction reaches equilibrium, making it reversible, so Na_2SiO_3 is converted back to SiO_2. This phenomenon can be proven by finding the equilibrium constant value using the reaction equation: $K_P = K_c\,(0{,}0821T)^{\Delta n}$, with the explanation: Kp = Gas equilibrium constant, Kc = Reaction equilibrium constant, T = Temperature (Kelvin), and Δn = Change in reaction moles.

After calculations, it was found that the value of Kp is 4.70, and after further calculations, the value of Kc was found to be 0.135. It is known that the value of Kc << 1, so if the reaction has reached equilibrium, the reaction will shift to the left (reactants) [18].

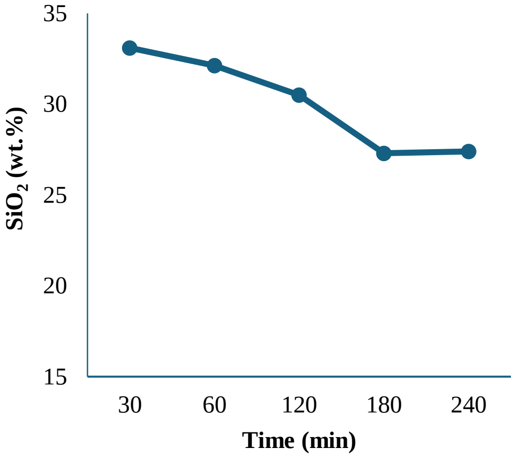

Figure 2. Effect of time on SiO_2 removal

It can be concluded that after an equilibrium time of 3 hours, the reaction will shift towards the reactants, increasing the mass of SiO_2.

3.2.2 Effect of Mass Ratio on Removal of SiO_2

The effect of mass ratio on the removal of SiO_2 after alkaline fusion is shown in Fig. 3. The result is that after a mass ratio of 1:1, there was a significant decrease in SiO_2 to a mass ratio of 1:1.47 and an increase of 1:1.83. In Figure 3, there is an increase in SiO_2 content from a mass ratio of 1:0.6 to 1:1, which is inconsistent with the theory that adding a larger number of reactants results in a larger amount of product [18]. However, after the mass ratio of 1:1, there is a significant decrease in SiO_2 content until the mass ratio of 1:1.47, followed by an increase at 1:1.83.

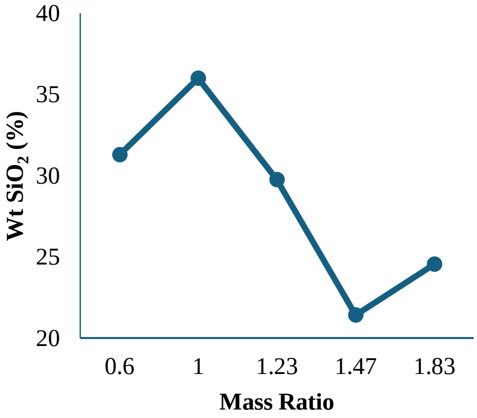

Figure 3. Effect of mass ratio on SiO_2 removal

The significant removal at 1:1.47 occurs because, according to stoichiometric reactions, the moles needed to react with 1 mole of SiO_2 are 2 moles of NaOH or a mass ratio of 1:1.32. At the mass ratio of 1:1.47, the stoichiometric reaction is 1:2.2 moles, so it can be assumed that SiO_2 is converted optimally or the reaction has reached equilibrium. After 1:1.47, there is an increase in SiO_2 content because the reaction is reversible, leading to a tendency for Na_2SiO_3 to form SiO_2. This phenomenon is evidenced by the value of Kc >> 1, where, according to Le Chatelier's principle, if the value of Kc >> 1 after the reaction reaches equilibrium, then with the addition of NaOH, the reaction will shift to the left (reactants) [18].

3.3 Acid Leaching

3.3.1 Effect of Leaching Time on Percent Extraction

Figure 4 shows the effect of time on percent extraction. Acid leaching occurs relatively quickly because lanthanum has a relatively high electronegativity [2], which allows it to easily release electrons and dissolve in H_2SO_4.

In Figure 4, it is observed that the longer the leaching time, the lower the extraction percentage, but this does not occur at a temperature of 90 °C. To determine the effect of leaching time, it is necessary to determine the Kc value, which can be expressed with the equation:

$$K_c = \frac{[La_2(SO_4)_3][H_2O]^6}{[H_2SO_4]^3[La(OH)_3]^2}$$

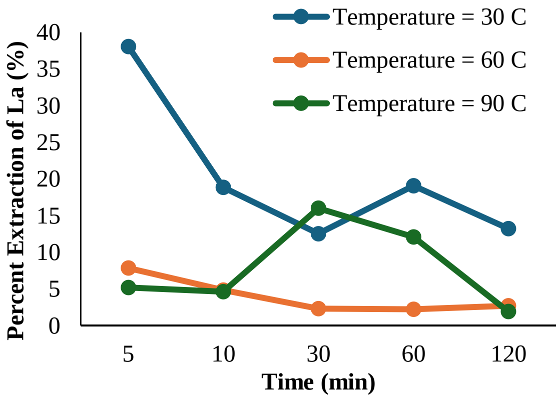

Figure 4. Effect of leaching time on the percent extraction of Lanthanum

After the calculations were performed, it was found that the Kc value was 21.33. If the value of Kc >> 1, then when the reaction reaches equilibrium, the reaction will shift to the right (products) [18]. Additionally, the obtained results do not align with the principle of reaction rate, which states that "reactants decrease over time while products increase over time," as shown in equation [18]. Figure 4 shows that lanthanum leaching occurs relatively quickly because lanthanum has a relatively high electronegativity [2], making it easy to release electrons and thus dissolve in H_2SO_4. The electronegativity of lanthanum is 1.117 [19].

In Figure 4, it is known that the longer the time, 5 minutes is the best time for leaching at temperatures of 30 and 60 °C, but this does not occur at 90 °C because at 90 °C the Si content in the filtrate is higher compared to 30 and 60 °C. The filtrate's Si content at 30 to 90 °C is 59490, 27796, and 73193 ppm, respectively. The research concluded that the best time for lanthanum leaching is 5 minutes, so this time was set as the time for subsequent leaching.

3.3.2 Effect of Temperature on Percent Extraction

Leaching was carried out by varying the temperature to 30, 60, and 90 °C, and the leaching time was 5 minutes, S/L 1/10, stirring rate 200 rpm, and H_2SO_4 concentration of 1 M. The Effect of temperature on percent extraction is shown in Fig. 5. Increasing temperature decreases the percentage of lanthanum extraction. This phenomenon is due to the solubility value. The solubility value of the product ($La_2(SO_4)_3$) decreases with increasing temperature. The solubility values of the product, respectively, from 30 to 90 °C, are 1.90, 1.26, and 0.79 [20]. Consequently, it can be determined that the optimal temperature for lanthanum leaching is 30 °C.

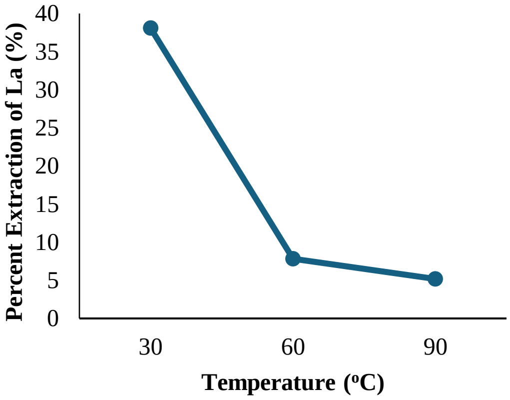

Figure 5. Effect of leaching temperature on the percent extraction of Lanthanum

3.3.3 Effect of H_2SO_4 Concentration on Percent Extraction

The leaching process occurs at 30 °C, utilizing a solid-to-liquid ratio of 1:10, a duration of 5 minutes, an agitation speed of 200 rpm, and H_2SO_4 concentrations of 1, 2, and 3 M.

Figure 6 shows the effect of concentration on percent extraction**.** The higher the concentration of H_2SO_4**,** the lower the percentage of lanthanum extraction.

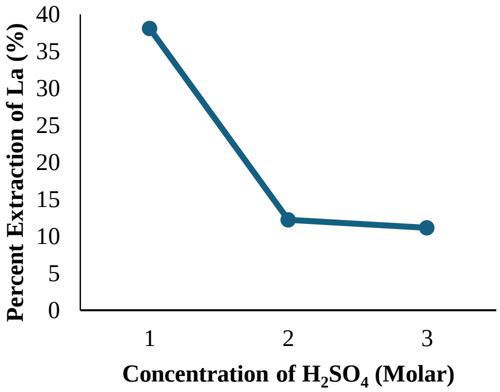

Figure 6. Effect of leaching concentration on the percent extraction of Lanthanum

Figure 6 illustrates that an increase in H_2SO_4 concentration correlates with a decrease in the percentage of lanthanum extraction. The results obtained in this study do not align with the research on the leaching of La from red mud using H_2SO_4 reagent, where a lower pH of the solution used leads to a decrease in extraction percentage [10].

The calculation was performed using equation [18]: $pH = -\log[H^+]$. The H^+ is the concentration of H_2SO_4 used. Thus, the pH presented in Table 3 is obtained. It can be concluded that the best leaching was done at an H_2SO_4 concentration of 1 M.

Table 3. Convert concentration to pH

H2SO4 Concentration	pH
1	-0.30
2	-0.60
3	-0.77

4. CONCLUSION

The duration of alkali fusion time and the slag: NaOH mass ratio affect the influence of SiO_2. The largest decrease in alkali fusion time of 3 hours is from 48.347% to 27.3%, and in the mass ratio of 1:1.47, it is from 48.347% to 21.413%. Time, temperature, and concentration influence the leaching of lanthanum. The duration of time inversely affects the extraction percentage, except for a temperature of 90 °C. The impact of temperature is such that an increase in temperature results in a decrease in extraction percentage. The impact of concentration is that an increased concentration results in a diminished extraction percentage. The optimal leaching point is at 5 minutes, 30 °C, and 1 M, resulting in a lanthanum extraction percentage of 38.082%.

ACKNOWLEDGMENT

The author expresses gratitude to the Hydrometallurgical Laboratory, Research Center for Metallurgy, BRIN Serpong, for offering facilities and valuable suggestions during the research process.

REFERENCES

[1] A. B. Prasetyo, A. Khaerul, W. Mayangsari, E. Febriana, A. Maksum, J. Andinie, F. Firdiyono, J.W. Soedarsono*et al.*, "Magnesium extraction of ferronickel slag processed by alkali fusion and hydrochloric acid leaching," *Journal of Mining and Metallurgy, Section B: Metallurgy*, vol. 57, no. 2, pp. 225-233, 2021. DOI: 10.2298/JMMB200224018P.

[2] F. R. Mufakhir, M. Z. Mubarok, and Z. T. Ichlas, "Leaching of silicon from ferronickel (FeNi) smelting slag with sodium hydroxide solution at atmospheric pressure," *IOP Conf Ser Mater Sci Eng*, vol. 285, 2018. DOI: 10.1088/1757-899X/285/1/012003.

[3] A. B. Prasetyo, A. Maksum, J. W. Soedarsono, and F. Firdiyono, "Thermal characteristics of ferronickel slag on roasting process with addition of sodium carbonate (Na_2CO_3)," *IOP Conf Ser Mater Sci Eng*, vol. 541, no. 1, 2019. DOI: 10.1088/1757-899X/541/1/012037.

[4] K. Trinopiawan, M. Z. Mubarok, J. Mellawati, and B. Y. Ani, "Pelindian logam tanah jarang dari terak timah dengan asam klorida setelah proses fusi alkali," *Eksplorium*, vol. 37, no. 1, p. 41, 2016. DOI:10.17146/Eksplorium.2016.37.1.2719.

[5] G. K. Gupta and N. Krishnamurthy, "Extractive metallurgy of rare earths," *International Materials Reviews*, vol. 37, no. 1, pp. 197-248, 1992. DOI: 10.1179/IMR.1992.37.1.197.

[6] N. Saleh, I. Rodliyah, S. Rochani, "Eliminasi senyawa silika dari terak peleburan timah menggunakan asam fluoro-silikat silica elimination from tin slags by fluoro-silicic acid leaching," *Jurnal Teknologi Mineral dan Batubara*, vol. 11, no. 2, 2015. DOI:10.30556/JTMB.VOL11.NO2.2015.710.

[7] C. Subramanian and A. Suri, "Recovery of niobium and tantalum from low grade tin slag-A hydrometallurgical approach," *Environmental & Waste Management in Non-Ferrous Metallurgical Industries*, pp. 100-107, 1998.

[8] G. Prameswara, I. Trisnawati, H. Poernomo, P. Mulyono, A. Prasetya, and H. T. B. M. Petrus, "Kinetics of yttrium dissolution from alkaline fusion on zircon tailings," *Min Metall Explor*, vol. 37, no. 4, pp. 1297-1305, 2020. DOI: 10.1007/S42461-020-00220-X/Figures/8.

[9] W. Astuti, N. M. Prilitasari, Y. Iskandar, D. Bratakusuma, and H. T. B. M. Petrus, "Leaching behavior of lanthanum, nickel and iron from spent catalyst using inorganic acids," *IOP Conf Ser Mater Sci Eng*, vol. 285, no. 1, 2018. DOI: 10.1088/1757-899X/285/1/012007.

[10] Abhilash, S. Sinha, M. K. Sinha, and B. D. Pandey, "Extraction of lanthanum and cerium from Indian red mud," *Int J Miner Process*, vol. 127, pp. 70-73, 2014. DOI: 10.1016/J.Minpro.2013.12.009.

[11] W. Mayangsari, A. B. Prasetyo, E. Febriana, J. Irawan, R. Subagja, F. Firdiyono, and J. W. Soedarsono, "The effect of roasting prior to the leaching process of alkalinized ferronickel slag followed by precipitation process," *Metalurgi*, vol. 36, no. 2, 2021. DOI: 10.14203/Metalurgi.V36I2.588.

[12] F. Gu, Z. Peng, Y. Zhang, H. Tang, L. Ye, W. Tian, G. Liang, J. Lee, M. Rao, G. Li, and T. Jiang, "Thermodynamic characteristics of ferronickel slag sintered in the presence of magnesia," *Minerals, Metals and Materials Series*, pp. 379-388, 2019. DOI: 10.1007/978-3-030-05749-7_38/Figures/8.

[13] W. Mayangsari, I. N. Avifah, A. B. Prasetyo, E. Febriana, A. Maksum, R. M. Ulum, F. Firdiyono, R. Subagja, J. W. Soedarsono "Decomposition of ferronickel slag through alkali fusion in the roasting process," *Eastern-European Journal of Enterprise Technologies*, vol. 2, no. 12-110, pp. 44-51, 2021. DOI: 10.15587/1729-4061.2021.217579.

[14] Y. Huang, Q. Wang, and M. Shi, "Characteristics and reactivity of ferronickel slag powder," *Constr Build Mater*, vol. 156, pp. 773-789, 2017. DOI: 10.1016/J.Conbuildmat.2017.09.038.

[15] F. Gu, Y. Zhang, Z. Peng, Z. Su, H. Tang, W. Tian, G. Liang, J. Lee, M. Rao, G. Li, T. Jiang, "Selective recovery of chromium from ferronickel slag via alkaline roasting

followed by water leaching," *J Hazard Mater,* vol. 374, pp. 83-91, 2019. DOI: 10.1016/J.Jhazmat.2019.04.002.

[16] D. Fang, J. Xue, and L. Xuan, "Recycling SiO_2 and Al_2O_3 from the laterite nickel slag in molten sodium hydroxides," *Minerals, Metals and Materials Series*, vol. Part F10, pp. 245-257, 2018. DOI: 10.1007/978-3-319-72138-5_25.

[17] M. D. Alfariz, W. Mayangsari, A. B. Prasetyo, A. Maksum, T. Prasetyo, R. M. Ulum, J. W. Soedarsono., "Effect of sodium carbonate (Na_2CO_3) additives and palm kernel shell charcoal to increase nickel and iron content from ferronickel slag using the pyrometallurgical method," *AIP Conf Proc*, vol. 2255, p. 0400341, 2020. DOI: 10.1063/5.0014052.

[18] R. Chang, "Chemistry essential concepts," *McGraw-Hill Companies, Inc.*, pp 210-230, 2010.

[19] J. H. L. Voncken, "The rare earth elements," pp 53-72, 2016. DOI: 10.1007/978-3-319-26809-5.

[20] J. A. Dean, "Lange's handbook of chemistry," *Materials and Manufacturing Processes*, vol. 5, no. 4, pp. 687-688, 1978. DOI: 10.1080/10426919008953291.

Metalurgi (2024) 2: 97 - 106

METALURGI
Majalah Ilmu dan Teknologi
p-ISSN 0126-3188 | e-ISSN 2443-3926
ejurnalmaterialmetalurgi.lipi.go.id

THE EFFECT OF SINGLE AND DOUBLE-DOPED ADDITION ON 8YSZ COATING LAYERS DEPOSITED ON INCONEL 625 BY ELECTROPHORETIC DEPOSITION

Kurotun Aini[1,2,*], Fina Fitratun Amaliyah[1], Eni Sugiarti[2], Resetiana Dwi Desiati[2], Nurul Latifah[2], Safitry Ramandhany[2], Ihah Fadilah[2], Aunillah Putri El Nasihah[2]
[1]Department of Physics, State Islamic University Sultan Maulana Hasanuddin Banten
Jl. Syech Nawawi Al-Bantani, Serang, Banten, Indonesia 42171
[2]Research Center for Advanced Materials, National Research and Innovation Agency
B.J. Habibie Sains and Technology Area, Banten, Indonesia 15314
*Email: kurotunaini44@gmail.com

Received: 31-1-2025, Revised: 18-06-2025, Accepted: 20-06-2025

Abstract

The ceramic layers of 8 mol% yttria-stabilized zirconia (8YSZ), singly doped with Fe_2O_3 and doubly doped with Fe_2O_3 and Al_2O_3, have been deposited successfully on Inconel 625 substrates by the EPD (electrophoretic deposition) process. The oxide doping influenced the stability of the EPD suspension and affected the density of the resultant layer. In order to improve the adhesion between the layer and the substrate, a two-step sintering was performed up to 1200 ºC for a total duration of 4 hours in a horizontal vacuum furnace, with a heating rate of 2 ºC per minute in an Argon gas atmosphere. FE-SEM (field emission scanning electron microscopy) and vickers hardness tests were employed to investigate the effect of single and double doping on the morphology and hardness of the coating layers, respectively. EDS (energy dispersive spectroscopy) was employed to analyze the elemental composition of the layers, while XRD (x-ray diffractometry) was utilized to determine the crystalline phases. The results indicated that the double-doped coating sample possesses a better microstructure and the layer with double doping exhibits a denser microstructure and reduced porosity (3.84%) in contrast to the single doping layer (6.05%). The vickers hardness test indicates a rise in hardness from 65.3 HV with single doping to 283.78 HV with double-doping layers, due to the presence of Al_2O_3 as the interstitial agent, which reduces the layer's porosity and enhances adhesion between the layer and the substrate. Furthermore, the addition of Al_2O_3 as the double dopant may impede the t → m phase transformation, leading to enhanced thermal stability in the double-doped coating sample compared to the single-doped coating sample. This study shows that double doping techniques can improve the efficiency of ceramic coatings for high-temperature applications, such gas turbine components, and also giving opportunities for more research in oxidation, corrosion, and erosion testing.

Keywords: *Al_2O_3, electrophoretic deposition, Fe_2O_3, inconel 625, yttrium-stabilized zirconia*

1. INTRODUCTION

Nickel-based superalloys, such as Inconel 625, are commonly used for parts that function at high temperatures, including gas turbine blades and aircraft vanes, due to their remarkable mechanical properties at high temperatures [1]. Nevertheless, prolonged exposure to such high temperatures frequently results in degradation caused by the passage of hot combustion gases that oxidize the components. Consequently, TBC (thermal barrier coatings) are often used as an insulation layer on nickel-based hot parts to enhance the component lifetime and improve efficiency [1]-[7].

The ceramic-based top layer in the TBC system has continual improvements regarding materials and coating techniques. The top layer typically consists of yttria-partially stabilized

DOI: 10.55981/metalurgi.2024.770

Metalurgi is Sinta 2 Journal (https://sinta.kemdikbud.go.id/journals/profile/3708) accredited by Ministry of Education, Culture, Research, and Technology, Republic Indonesia

zirconia, due to its exceptional characteristics, including low thermal conductivity and a high thermal expansion coefficient, which are nearly acceptable with superalloys [2]. Yttria-stabilized zirconia (YSZ) is commonly used as the topmost layer by techniques such as EB-PVD (electron beam physical vapor deposition), APS (air plasma spraying), or CVD (chemical vapor deposition) [3].

Established methods have been widely employed for the creation of YSZ layers. Nonetheless, the intricacy of the required equipment, production expenses, and restricted adaptability have emerged as concerns [4]. Other studies have taken efforts to create a simple, flexible, and cost-effective coating technique [7]. This process is known as EPD (electrophoretic deposition). The EPD technique is a cost-effective and straightforward alternative to create simple, versatile, and economical coatings. This technique facilitates the uniform deposition of charged ceramic particles from a liquid suspension onto the surface of a conductive substrate via an electric field [5]-[6].

The suspension stability, electric source, and deposition duration are parameters that may affect the characteristics of the layer deposited with the EPD method [9]-[10]. The ideal coating suspension must be metastable, allowing dissolved particles to adhere to the substrate without excessive sedimentation in the bath [9]. The rate of deposition increases as voltage rises. Nonetheless, the use of high voltage may create a substantial electric field, which could compromise the coating quality beyond a certain threshold. High-voltage application can lead to the rapid deposition of ceramic particles onto the substrate. This may impact deposition quality and result in layers with uneven structures, leading to porosity and the formation of cracks [10]. Consequently, an optimal voltage application is necessary for the deposition of ceramic particles, which, according to the literature, occurs at a voltage below 100 V [9]. In addition, the duration of deposition affects the thickness of the YSZ layer produced by EPD. Bai et al., [7] revealed that the ideal duration for the EPD process utilizes a voltage gradient of 3 to 15 minutes, during which the voltage gradient method for coating typically results in a YSZ layer thickness of 300-400 μm .

The freshly coated YSZ ceramic layer requires sintering to promote recrystallization, increase layer density, and enhance adhesion between the layer and substrate [3]. The temperature necessary for the YSZ densification must exceed 1300 ºC, due to the high melting point of YSZ [11]. Schulz et al. performed sintering on YSZ layers at temperatures ranging from 1200 to 1400 ºC [12]. The results indicated that during single-stage sintering, a combination of tetragonal (t) and cubic (c) phases, as well as several monoclinic (m) phases, were formed. The existence of the m-phase after sintering at 1400 ºC is detrimental due to its potential to induce thermal stress. The stress induced by cooling during the t→m phase transformation will impact the durability of the coating system [12]. Consequently, additional elements or oxide doping are required to control the t→m phase transformation and maintain the capacity to reduce the sintering temperature.

The investigation of various additives, such as CoO, CuO, Fe_2O_3, Bi_2O_3, SiO_2, Al/Al_2O_3, ZrN, Sc_2O_3, and Ni/NiO, has been conducted to lower the sintering temperature of the YSZ layer [9], [14]-[15]. Kalinina et al. indicated that the addition of Al_2O_3 into the YSZ suspension during deposition by the EPD method produced a dense and uniform layer with minimal porosity after sintering at 1200 °C [14]. In addition, Bai et al., [7] demonstrated that Fe_2O_3 serves as a proficient sintering aid, lowering the sintering temperature of refractory ceramics and enhancing the densification of tetravalent oxides, including ZrO_2. Consequently, it can be inferred that employing Al_2O_3 and Fe_2O_3 as individual oxide dopants may improve the microstructure of the YSZ layer by distinct enhancement processes.

Guo et al., [15] investigated the YSZ coatings with Fe_2O_3 as a single dopant. Their findings demonstrated that the addition of Fe_2O_3 doping into the 3YSZ layer enhances the grain size; nevertheless, the enhancement is insignificant, resulting in a less dense layer structure, with ceramic phase instability perhaps serving as a contributing factor. In contrast, the use of double or multiple doping on the ZrO_2 coating is recognized to produce a ZrO_2 ceramic layer with remarkable phase stability. The addition of Al_2O_3, CeO_2, Yb_2O_3, and Gd_2O_3 via the APS method on ZrO_2 coating is recognized to substantially reduce phase transition, enhance thermal stability, and improve bond strength [16]. Consequently, it can be inferred that double oxide doping possesses significant potential as a sintering agent that enhances the microstructure of the YSZ layer.

The use of double oxide doping on YSZ layers via the EPD method is recognized as constrained and under-researched. This study aims to investigate the impact of single (Fe_2O_3) and double (Fe_2O_3+Al_2O_3) oxide doping on 8YSZ layers in relation to microstructure, layer porosity, surface hardness, phase formation, and phase stability to evaluate its efficacy as a protective layer for Inconel 625 substrates. In addition, the flow behavior of various 8YSZ suspensions using the EPD method was observed to comprehend the properties of the 8YSZ suspension affected by oxide doping. Consequently, a comprehensive examination of the impact of oxide doping on the development of the 8YSZ layer may be conducted.

2. MATERIALS AND METHODS

2.1 Sample Preparation

The present study utilized Inconel 625 (Nilaco, Japan) with dimensions of 15 x 15 x 1 mm as a substrate. With the chemical composition of Inconel 625 in wt.% such as: (20-23)Cr, (8-10)Mo, 5Fe, (3.15-4.15)Nb+Ta, 1Co, 0.5Mn, 0.5Si, 0.4Al, 0.4Ti, 0.1C, 0.015P, 0.015 S, with Ni as the balance. The substrate was polished in succession with SiC paper of grit sizes 100, 500, and 800. The substrate was ultrasonically cleaned in acetone for 180 seconds following polishing.

Table 1. Mass percentage composition of the analyzed suspension (wt.%)

Materials	Single-doping suspension	Double-doping suspension
8YSZ	94.52	86.4
Fe_2O_3	0.76	0.7
Al_2O_3	-	8.6
Iodine	4.73	4.3
Acetyl acetone	50	50
Ethanol	50	50

This study created two types of 8YSZ suspensions for coating via the EPD procedure to investigate the impact of the oxide doping addition method: single-doping suspension and double-doping suspension, as detailed in Table 1. The suspension was prepared by mixing the commercial 8YSZ powder (8 mol% Y_2O_3, >99%, Kanto, Japan), Iron (III) Oxide (0.02 mol% Fe_2O_3, >99%, technical powder), Aluminum Oxide (Al_2O_3 powder, Kanto Chemical Co., Inc.), and iodine as a dispersant in a solvent. Acetyl acetone (ACAC, >99%, Merck) and ethanol (Et>99%, Merck) were utilized as the solvent in a 1:1 volume ratio. A viscosity test was conducted using the ViscoQC100 rotational viscometer on days 1, 2, 3, 4, and 8 to evaluate the stability and adequacy of the suspension for the deposition process. This test evaluates the flow properties of fluid viscosity and assesses the stability of the suspension for the deposition process using EPD.

2.2 EPD Procedure

Before the implementation of EPD, the suspension was mixed using a magnetic stirrer followed by sonication for 5 minutes. This study employed a cathodic EPD process using a nickel plate as the anode and Inconel 625 as the cathode, with a distance of approximately 3 cm between the anode and cathode, as illustrated in Figure 1(a).

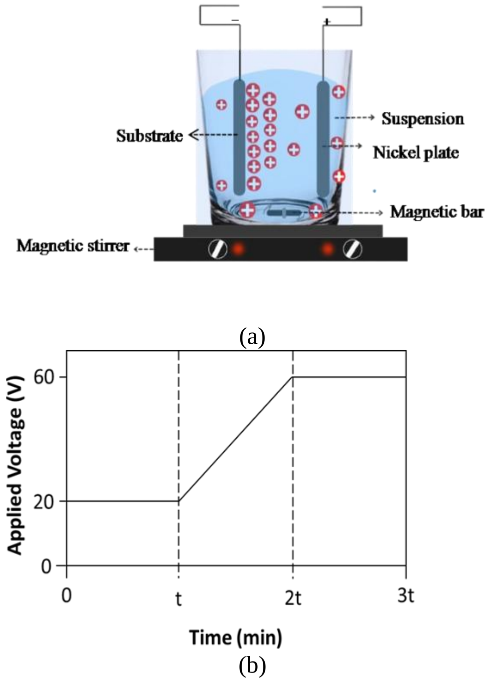

(a)

(b)

Figure 1. Schematic representation of (a) the EPD process and (b) the applied voltage

The DC power supply (XANTREX, XHR 60-18) was used as the voltage source for the EPD process. The voltage treatment was conducted using a two-stage parameter, consisting of a constant voltage (20 V), a gradient voltage (20-60 V), and a final constant voltage (60 V), with a total duration of 12 minutes, as depicted in Fig. 1(b).

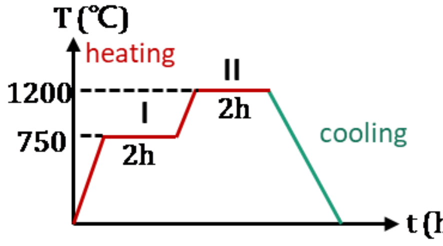

Figure 2. Schematic of the sintering profile

The freshly coated sample was dried at room temperature for 24 hours and then sintered in a horizontal vacuum furnace with a heating rate of 2 °C per minute in an Argon atmosphere.

Sintering was performed in two stages: the initial stage at 750 °C for 2 hours, followed by a second stage at 1200 °C for 2 hours. Figure 2 illustrates the schematic representation of the two-stage sintering profile.

2.3 Characterization

The coating samples were analyzed using field emission-scanning electron microscopy (FE-SEM, JEOL, JIB4610F) combined with EDS (energy dispersive spectroscopy), Oxford, X-Max 50 mm^2 to study the elemental composition and examine the surface and cross-sectional microstructure. Analysis of cross-sectional images using ImageJ software was conducted to evaluate the porosity of the layer. The XRD (x-ray diffraction) SmartLab, Rigaku employs Cu Kα radiation (wavelength, 1.5405 Å), operating at 40 kV and 30 mA, with a 2θ range of 10° to 90° to identify the phases present in the coating. Subsequently, to assess the mechanical properties of the coating, the surface hardness of the coating samples was evaluated utilizing a hardness tester (Mitech, MH600).

3. RESULTS AND DISCUSSION

3.1 Viscosity of the YSZ Suspension

In the EPD process, particles will migrate towards the liquid phase upon the application of an electric field. Consequently, several suspension parameters need to be considered throughout the coating process utilizing the EPD method, including a high dielectric constant, low conductivity, and low viscosity. The viscosity of the suspension was observed on the first, second, third, fourth, and eighth days to analyze the progression of viscosity and the flow characteristics of the suspension over time[9]. The viscosity on the eighth day demonstrates optimal stability according to the daily viscosity measurements.

Figure 3 shows that the viscosity of the 8YSZ double-doping suspension is notably higher than that of the single-doping suspension, with values ranging from 0.928 to 1.031 m.Pa.s for single doping and from 0.979 to 1.288 m.Pa.s for double doping. Both suspensions have low viscosity values and comparable flow behavior curves, specifically demonstrating shear-thinning characteristics. Upon closer examination, the flow behavior curve of the double-doping suspension appears to be more unstable than that of the single-doping suspension. This is beneficial because, if the suspension is excessively stable, the repulsive forces among the particles will not be overcome by the electric field, hence inhibiting deposition. Some models for EPD indicate that the suspension should be unstable in proximity to the electrodes [9].

The instability of the double-doping suspension can be attributed to the presence of Al_2O_3. Al_2O_3 is an acidic oxide that can absorb free oxygen ions, leading to a tetrahedral structure of four-coordinate aluminum oxide, which enhances viscosity and creates a well-dispersed solution [18]. Therefore, it can be concluded that the double-doping suspension exhibits ideal conditions for deposition using the EPD method, with a viscosity value of 1.09 mPa.s as the reference [8].

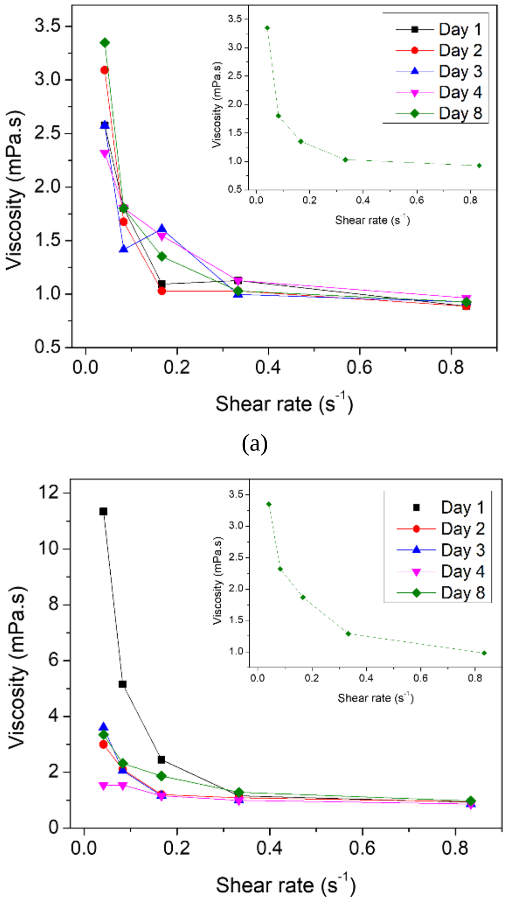

(a)

(b)

Figure 3. Correlation between shear rate and viscosity of 8YSZ suspension: (a) single-doping, and (b) double-doping

3.2 Coating Morphology

Figure 4 shows the cross-sectional image and elemental mapping of the various 8YSZ coating samples influenced by oxide doping. The 8YSZ layer was applied on Inconel 625 via the EPD method and subjected to a two-stage sintering process up to 1200 °C for a total duration of 4 hours. EDS measurements indicated a strong signal of nickel (Ni), chromium (Cr), and molybdenum (Mo), confirming the Inconel 625 substrate composition. In addition, it was observed that the coating layers consisted of two layers: a ceramic layer and an oxide layer. The ceramic layer consisted of zirconium (Zr), yttrium(Y), and oxygen (O), confirming the YSZ composition, whereas the oxide layer consisted of Cr and O elements, indicating the formation of chromium oxide between the substrate and coating layer.

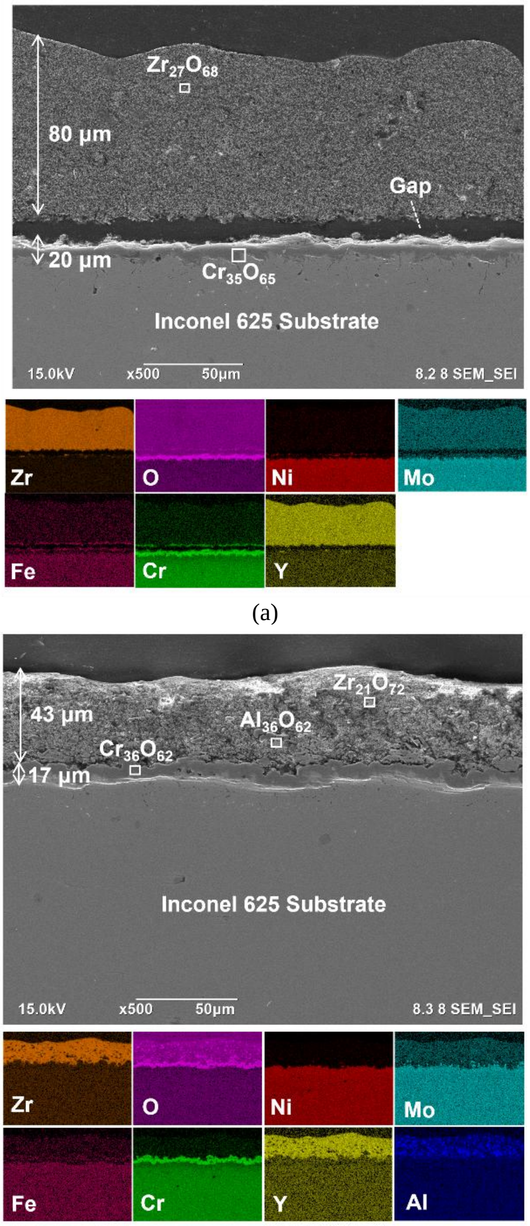

(a)

(b)

Figure 4. Cross-sectional morphology of the 8YSZ coating samples:(a) single-doping, and (b) double-doping

The coating sample with single doping creates a zirconia layer thickness of approximately 80 µm, whereas the coating sample with double doping results in a thickness of 43 µm. The top coat of zirconia consisted of Zr and O elements with atomic percentages (at%) ranging from 21 to 27 and 68 to 72, respectively. In addition, the oxide layer formed with a thickness of approximately 20 µm for coating samples with single doping and 17 µm for those with double doping. The oxide layer of chromia consisted of Cr and O elements with atomic percentages (at.%) ranging from 35 to 36 and 62 to 65, respectively. The oxide layer of the two coating samples has been characterized as thermally grown oxide (TGO), with its formation caused by the diffusion of metal ions (Cr^{3+}) from the substrate and the ingress of oxygen ions (O^{2-}) due to elevated temperatures [19].

Furthermore, the single-doped coating sample shows a uniform layer with barely visible pores. Nonetheless, there are gaps between the YSZ ceramic layer and the TGO. Defects like pores and gaps in the coating layer may arise due to the volume shrinkage effect of the upper layer during prolonged high-temperature sintering [7]. In contrast, the double-doped coating samples exhibit a dense layer characterized by reduced porosity. This could be attributed to the addition of Al_2O_3, which functions as an interstitial agent that diminishes the layer's porosity. Furthermore, Al_2O_3 possesses a high melting point, suggesting it is appropriate as a binding agent for ceramics subjected to high sintering temperatures [20]. The addition of Al_2O_3 can reduce the volumetric shrinkage of the coating and improve its adhesion to the metallic substrate. The volumetric expansion from the metal-ceramic reaction partially offsets the sintering shrinkage, facilitating the creation of a ceramic layer with minimal shrinkage [11]. Consequently, the presence of Al_2O_3 can improve the adhesion between the layer and the substrate.

3.3 Surface Morphology

Figure 5 shows the surface morphology of the various 8YSZ coating samples influenced by oxide doping. The surface morphology of the single-doped coating sample exhibits enhanced grain growth, indicated by larger grain sizes than the double-doped coating sample. The high diffusion coefficient of Zr^{4+} is primarily responsible for the rapid densification rate of the Fe_2O_3 on the 8YSZ layer, due to the interstitial diffusion mechanism of Fe^{3+} ions resulting from the simultaneous presence of substitutional and interstitial Fe^{3+} ions [15].

Single doping influences the surface morphology of the 8YSZ layer by promoting an increase in grain size. Simultaneously, the surface morphology of the 8YSZ layer with double doping exhibits reduced grain growth. The addition of Al_2O_3, which reinforces the ZrO_2 ceramic layer interstitially, leads to increased layer hardness and reduced porosity. Kalinina et al., [14] discovered that the addition of Al_2O_3 in the EPD suspension during YSZ deposition results in a dense and homogeneous layer with reduced porosity, therefore, Al_2O_3 serves to enhance the hardness of a layer. In addition, vacancies exist in both single-doped and double-doped coating samples. Nevertheless, the single-doped coating samples exhibit larger voids compared to the double-doped coating samples.

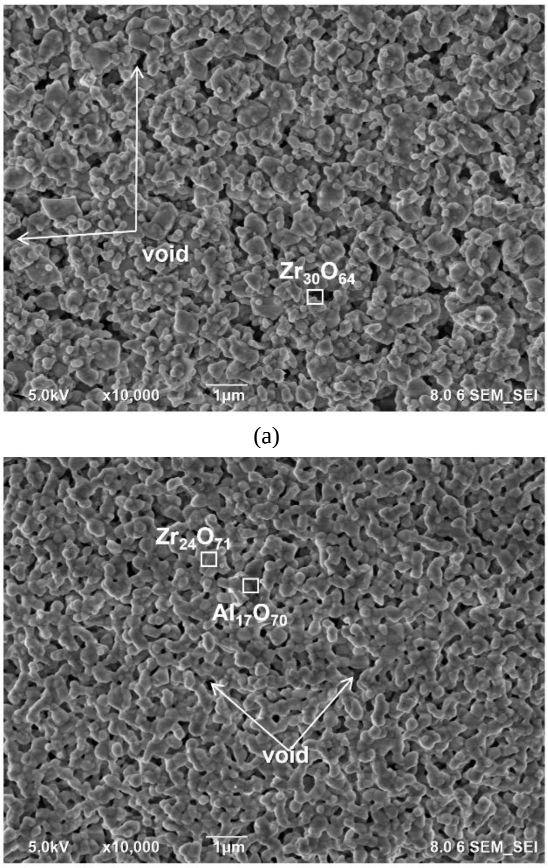

(a)

(b)

Figure 5. Surface microstructure of the 8YSZ coating sample: (a) single-doping, (b) double-doping

This may relate to the function of Al_2O_3 as an interstitial agent in reducing voids. Layers with fewer voids might improve the adherence of the layer. Excessive void content in a coating can diminish the material's strength, as big voids may serve as susceptible areas that facilitate additional damage, including gaps and cracks. Cracks develop in regions with voids resulting from the pressure exerted on the material. Moreover, exposure to high temperatures will result in increased volumetric expansion, potentially leading to the formation of gaps between the coating and the substrate, as illustrated in Fig. 4(a).

3.4 Surface Hardness and Porosity

Figure 6 shows the effect of oxide doping on the surface hardness and porosity of the 8YSZ coating samples. Furthermore, the data about surface hardness and porosity are presented in Table 2.

The results indicate that the double-doped coating sample demonstrates the highest surface hardness of 283.8 ± 2.13 HV and the lowest porosity of 3.84 ± 0.05 %. The increase in surface hardness is due to grain refinement, which reduces porosity during the sintering process.

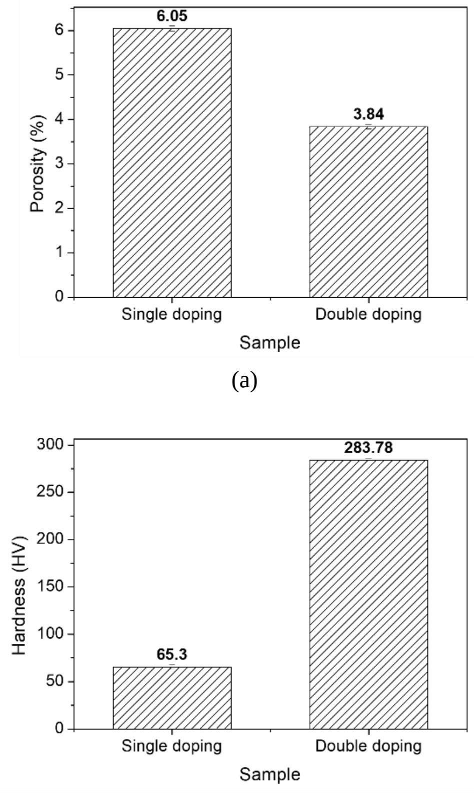

(a)

(b)

Figure 6. (a) Porosity, and (b) surface hardness of the 8YSZ coating sample

The use of Al_2O_3 might improve hardness by acting as a reinforcing phase dispersed throughout the coating layer. The Al_2O_3 interstitially enhances the densification of the ZrO_2 ceramic layer, thus improving the surface hardness.

Table 2. Surface hardness and porosity data of the coating samples

Coating Sample	Porosity (%)	Surface Hardness (HV)
Single-doped	6.05 ± 0.06	65.3 ± 2.31
Double-doped	3.84 ± 0.05	283.78 ± 2.13

The use of double doping on the 8YSZ layer significantly improved surface hardness from 193.8 HV, as reported by Khanali et al., [21].

3.5 Phase Analysis

Figure 7 shows the diffraction patterns of the coating samples subjected to single and double doping. Through the reference ICSD (inorganic crystal structure database), the phases formed in both layers were obtained, namely the tetragonal Zirconia phase (t-ZrO_2) with reference code (ICSD-98 065-5671) and the monoclinic Zirconia phase (m-ZrO_2) with reference code (ICSD-98-006-0900).

Analysis of the Rietveld refinement results shows that the crystal size in the single-doping sample is 51.1 nm, while in the double-doping sample it decreases to 30.54 nm. This decrease indicates that the combination of Fe_2O_3 and Al_2O_3 dopants is capable of inhibiting crystal growth during the coating process, resulting in a finer and denser microstructure [22]. Additionally, the goodness of fit (GoF) value obtained from the refinement results indicates a better model structure fitting quality to the experimental data in the double-doped samples. The GoF for the single doping sample is 1.67939, while the double doping has a lower GoF of 1.45673, reflecting an improvement in the accuracy of the simulated crystal model. The resulting lattice parameters show significant changes due to variations in doping types, both in the tetragonal and monoclinic phases of ZrO_2. In the single doping sample, the tetragonal phase lattice parameters were recorded as a = b = 3.62877 Å and c = 5.17936 Å, while the monoclinic phase showed a = 5.157 Å, b = 5.21128 Å, and c = 5.28903 Å. Meanwhile, in the double doping, the tetragonal phase lattice parameters slightly increased along the a and b axes to 3.63423 Å, with a decrease along the c axis to 5.14794 Å. For the monoclinic phase, the lattice parameters shifted to a = 5.151 Å, b = 5.203 Å, and c = 5.316 Å. The change in lattice parameters indicates that double doping causes a more significant distortion in the crystal structure compared to single doping.

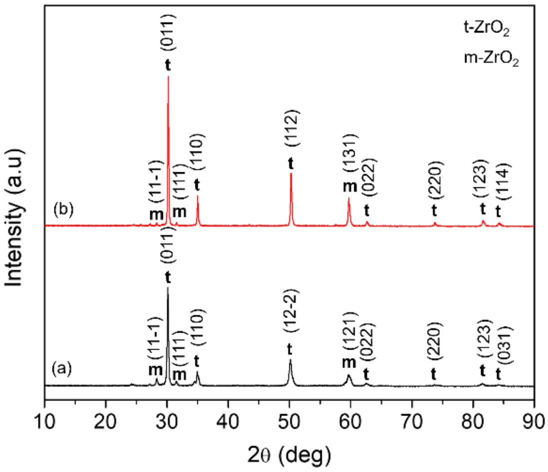

Figure 7. XRD pattern of 8YSZ coating sample: (a) single-doping, and (b) double-doping

The addition of Al_2O_3 as a double-doped could enhance the prevalence of the tetragonal zirconia phase, as demonstrated in Table 3.

The use of Al_2O_3 in the double-doped coating sample may improve the stability of the tetragonal zirconia (t-ZrO_2) phase by being interstitially located in the grain boundaries and impeding the t→m phase transformation. The t-ZrO_2 phase in this coating sample is beneficial due to its superior thermal stability compared to the monoclinic zirconia (m-ZrO_2) phase.

Table 3. Percentages (%) of monoclinic (m) and tetragonal (t)-ZrO_2 phase

Coating Sample	**m-ZrO_2**	**t-ZrO_2**
Single-doped	16. 1	83. 9
Double-doped	3. 8	96. 2

Consequently, the double-doped coating sample exhibits superior phase stability compared to the single-doped coating sample. A substantial percentage of the m-ZrO_2 phase may compromise the coating due to reduced stability of the zirconia ceramic phase and the formation of micro and macro cracks caused by volumetric expansion. As a result, the coated sample with single doping may demonstrate insufficient resistance to high-pressure and temperature conditions. In contrast, the use of Al_2O_3 as a double-doped enhances the stability of the t-ZrO_2 by reducing defects, such as cracks or voids, thus protecting the coating and substrate under high-temperature conditions.

4. CONCLUSION

The present study aimed to investigate the microstructure, porosity, surface hardness, and phase formation of the 8YSZ layer with single doping and double doping, generated by the electrophoretic deposition method.The results showed that on the eighth day, the 8YSZ suspension achieved optimal viscosity, particularly in the double-doped suspension, which exhibited a range of 0.979–1.288 mPa.s and demonstrated favorable conditions for EPD due to higher instability. The cross-sectional microstructure of the double-doped coating sample revealed a denser and more compact layer than the single-doped counterpart, which can be attributed to the presence of Al_2O_3 as an interstitial agent that reduces porosity and enhances adhesion to the substrate. Surface morphology analysis showed reduced grain growth and minimal voids in the double-doped layer, resulting in low porosity (3.84 ± 0.05%) and high surface hardness (283.78 ± 2.13 HV). Furthermore, phase analysis confirmed the dominance of tetragonal ZrO_2, with a higher percentage of the t-ZrO_2 phase found in the double-doped sample, likely due to the suppression of the t→m phase transformation by Al_2O_3 addition, enhancing the thermal stability of the ceramic layer. These findings contribute significantly to the development of cost-effective and efficient thermal barrier coatings for applications such as gas turbine engines. Future work should include cyclic thermal fatigue, oxidation, and erosion testing to evaluate the long-term durability of the coating system under service conditions.

ACKNOWLEDGMENT

The authors would like to thank the Internal Program of the National Research and Innovation Agency (BRIN) with contract No. B-2/III.10/HK/2025 for financial support of this work.

REFERENCES

[1] K. Mondal, L. Nuñez, C. M. Downey, and I. J. Van Rooyen, “Thermal barrier coatings overview: Design, manufacturing, and applications in high-temperature industries,” *Ind. Eng. Chem. Res.*, vol. 60, no. 17, pp. 6061-6077, 2021. DOI: 10.1021/acs.iecr.1c00788.

[2] E. G. Kalinina and E. Y. Pikalova, “Preparation and Properties of Stable Suspensions of ZrO2–Y2O3 Powders with Different Particle Sizes for Electrophoretic Deposition,” *Inorg. Mater.*, vol. 56, no. 9, pp. 941–948, 2020. DOI: 10.1134/S0020168520090095.

[3] R. D. Desiati, A. Anawati, and E. Sugiarti, “Two-step sintering iImproved compaction of electrophoretic-deposited YSZ coatings,” *J. Mater. Eng. Perform.*, vol. 31, no. 12, pp. 9888-9899, 2022. DOI: 10.1007/s11665-022-07004-y.

[4] R. D. Desiati, A. Anawati, and E. Sugiarti, “Microstructural and mechanical characteristics of ceramic composite coating developed by electrophoretic deposition,” *IOP Conf. Ser. Mater. Sci. Eng.*, vol. 1098, no. 6, p. 062073, 2021. DOI: 10.1088/1757-899x/1098/6/062073.

[5] M. J. Zamharir, H. Aghajani, and A. T. Tabrizi, “Evaluation of adhesion strength of TiN layer applied on 316L substrate by electrophoretic deposition,” *J. Aust. Ceram. Soc.*, vol. 57, no. 4, pp. 1219-1230, 2021. DOI: 10.1007/s41779-021-00621-1.

[6] E. G. Kalinina and E. Y. Pikalova, “Electrophoretic deposition of dense anode barrier layers of doped ZrO_2 and $BaCeO_3$ on a supporting Ce0.8Sm0.2O2-δ solid electrolyte: Problems and search for solutions in SOFC technology,” *Int. J. Hydrogen Energy*, vol. 48, no. 59, pp. 22610-22623, 2023. DOI: 10.1016/j.ijhydene.2023.02.042.

[7] M. Bai, F. Guo, and P. Xiao, “Fabrication of thick YSZ thermal barrier coatings using electrophoretic deposition,” *Ceram. Int.*, pp. 1-10, 2014. DOI: 10.1016/j.ceramint.2014.08.021.

[8] H. Maleki-ghaleh, M. Rekabeslami, M. S. Shakeri, and M. H. Siadati, “Nano-structured yttria-stabilized zirconia coating by electrophoretic deposition,” *Appl. Surf. Sci.*, vol. 280, pp. 666-672, 2013. DOI: 10.1016/j.apsusc.2013.04.173.

[9] L. Besra and M. Liu, “A review on fundamentals and applications of electrophoretic deposition (EPD),” *Prog. Mater. Sci.*, vol. 52, pp. 1-61, 2007. DOI: 10.1016/j.pmatsci.2006.07.001.

[10] R. D. Desiati, A. Anawati, and E. Sugiarti, “Microstructural and mechanical characteristics of ceramic composite coating developed by electrophoretic deposition,” *Mater. Sci. Eng.*, pp. 1-6, 2021. DOI: 10.1088/1757-899X/1098/6/062073.

[11] Z. Wang, P. Xiao, and J. Shemilt, “Fabrication of composite coatings using a combination of electrochemical methods and reaction bonding process,” *J. Eur. Ceram. Soc.*, vol. 20, pp. 1469-1473, 2000. DOI:10.4236/jbise.2008.13032.

[12] U. Schulz, “Phase transformation in EB-PVD Yttria partially stabilized Zirconia thermal barrier coatings during annealing,” *J. Am. Ceram. Soc.*, vol. 83, no. 4, pp. 904-910, 2000.

[13] B. Baufeld and O. Van Der Biest, “Lowering the sintering temperature for EPD coatings by applying reaction bonding,” *J. Eur. Ceram. Soc.*, vol. 28, pp. 1793-1799, 2008. DOI: 10.1016/j.jeurceramsoc.2007.11.019.

[14] E. G. Kalinina, A. A. Efimov, and and A. P. Safronov, “Preparation of YSZ / Al_2O_3 composite coatings via electrophoretic deposition of nanopowders,” *Inorg. Mater.*, vol. 52, no. 12, pp. 1301-1306, 2016. DOI: 10.1134/S0020168516110054.

[15] F. Guo and P. Xiao, “Effect of Fe_2O_3 doping on sintering of yttria-stabilized zirconia,” *J. Eur. Ceram. Soc.*, vol. 32, no.

16, pp. 4157-4164, 2012. DOI: 10.1016/j.jeurceramsoc.2012.07.035.

[16] J. Wang, Y. Wang, M. Chen, C. Wang, Y. Yu, Y. Tian, B. Liu, and Q. Jing, “Degradation of CeO_2 and TiO_2 co-stabilized ZrO_2 by the V_2O_5 molten salts and Na_2SO_4 + V_2O_5 molten salts,” *Surf. Coatings Technol.*, vol. Volume 437, 2022. DOI: 10.1016/j.surfcoat.2022.128352.

[17] M. M. De Oliveira, A. A. Couto, G. F. C. Almeida, D. A. P. Reis, N. B. De Lima, and R. Baldan, “Mechanical behavior of inconel 625 at elevated temperatures,” *Metals (Basel)*, vol. 9, no. 3, 2019. DOI: 10.3390/met9030301.

[18] Q. Cheng, Z. Zhang, X. Xing, J. Zheng, and Y. She, “Effect of MgO/Al_2O_3 on viscosity and thermodynamic properties of high-Titanium slag containing chlorine,” *Minerals*, vol. 13, no. 444, pp. 2-13, 2023. DOI:10.3390/min13030444.

[19] D. R. Clarke and C. G. Levi, “Materials design for the next generation thermal barrier coatings,” *Annu. Rev. Mater. Res*, no. 33, pp. 383-417, 2003. DOI: 10.1146/annurev.matsci.33.011403.113718.

[20] A. Khezrloo, S. Baghshahi, M. R. Afshar, and A. A. Amadeh, “Sintering and thermal shock behavior of Yttria-stabilized Zirconia coating deposited by electrophoretic method on inconel 738LC superalloy,” *Trans. Indian Inst. Met.*, vol. 75, no. 10, pp. 2617-2627, 2022. DOI: 10.1007/s12666-022-02626-1.

[21] O. Khanali, M. Rajabi, and S. Baghshahi, “Effect of non-aqueous solvents on deposition properties in electrophoretic deposition process of yttria stabilized zirconia nano-powders,” *J. Ceram. Process. Res.*, vol. 18, no. 10, pp. 735-742, 2017.

[22] M. Thakur, A. Vij, F. Singh, and V. S. Rangra, “Spectroscopic studies of metastable tetragonal ZrO_2 nanocrystals,” *Spectrochim. Acta - Part A Mol. Biomol. Spectrosc.*, vol. 305, p. 123495, 2024. DOI: 10.1016/j.saa.2023.123495.

AUTHOR INDEX

SUBJECT INDEX